

# New Adaptive Numerical Methods Based on Dual Formulation of Hyperbolic Conservation Laws

Alina Chertock\*, Qingcheng Fu†, Alexander Kurganov‡, and Lorenzo Micalizzi§

## Abstract

In this paper, we propose an adaptive high-order method for hyperbolic systems of conservation laws. The proposed method is based on a dual formulation approach: Two numerical solutions, corresponding to conservative and nonconservative formulations of the same system, are evolved simultaneously. Since nonconservative schemes are known to produce nonphysical weak solutions near discontinuities, we exploit the difference between these two solutions to construct a smoothness indicator (SI). In smooth regions, the difference between the conservative and nonconservative solutions is of the same order as the truncation error of the underlying discretization, whereas in nonsmooth regions, it is  $\mathcal{O}(1)$ . We apply this idea to the Euler equations of gas dynamics and define the SI using differences in the momentum and pressure variables. This choice allows us to further distinguish neighborhoods of contact discontinuities from other nonsmooth parts of the computed solution. The resulting classification is used to adaptively select numerical discretizations. In the vicinities of contact discontinuities, we employ the low-dissipation central-upwind numerical flux and a second-order piecewise linear reconstruction with the slopes computed using an overcompressive SBM limiter. Elsewhere, we use an alternative weighted essentially non-oscillatory (A-WENO) framework with the central-upwind finite-volume numerical fluxes and either unlimited (in smooth regions) or Ai-WENO-Z (in the nonsmooth regions away from contact discontinuities) fifth-order interpolation. Numerical results for the one- and two-dimensional compressible Euler equations show that the proposed adaptive method improves both the computational efficiency and resolution of complex flow features compared with the non-adaptive fifth-order A-WENO scheme.

**Key words:** Smoothness indicator; adaptive methods; conservative and primitive formulations; Euler equations of gas dynamics.

**AMS subject classification:** 65M06, 76M20, 35L65, 76L05

---

\*Department of Mathematics, North Carolina State University, Raleigh, NC 27695, USA; [chertock@math.ncsu.edu](mailto:chertock@math.ncsu.edu)

†Department of Mathematics, Southern University of Science and Technology, Shenzhen, 518055, China; [12431005@mail.sustech.edu.cn](mailto:12431005@mail.sustech.edu.cn)

‡Department of Mathematics and Shenzhen International Center for Mathematics, Southern University of Science and Technology, Shenzhen, 518055, China; [alexander@sustech.edu.cn](mailto:alexander@sustech.edu.cn)

§Department of Mathematics, North Carolina State University, Raleigh, NC 27695, USA; [lmicali@ncsu.edu](mailto:lmicali@ncsu.edu)

# 1 Introduction

In this paper, we introduce new adaptive high-order numerical methods for hyperbolic systems of conservation laws within a dual formulation (DF) framework. In the two-dimensional (2-D) case, the governing equations can be expressed as

$$\mathbf{U}_t + \mathbf{F}(\mathbf{U})_x + \mathbf{G}(\mathbf{U})_y = \mathbf{0}, \quad (1.1)$$

respectively. Here,  $x$  and  $y$  denote spatial variables,  $t$  denotes time,  $\mathbf{U} \in \mathbb{R}^d$  is the vector of conserved variables, and  $\mathbf{F} : \mathbb{R}^d \rightarrow \mathbb{R}^d$  and  $\mathbf{G} : \mathbb{R}^d \rightarrow \mathbb{R}^d$  are nonlinear flux functions.

Hyperbolic systems of conservation laws often generate complex wave structures, including shock, rarefaction, and contact waves, even when the initial data are smooth. The numerical approximation of such systems is particularly challenging, as the schemes should not only maintain high accuracy in smooth regions but also capture discontinuous structures without producing spurious oscillations. Over the past decades, a wide range of numerical schemes for such systems have been proposed; see, e.g., monographs and review papers [23, 27, 36, 44, 45, 48].

It is well-known that in order to achieve high resolution of discontinuous solution structures on practically affordable meshes, one has to use numerical methods that are at least second-order accurate. Moreover, when the solution contains nontrivial smooth structures, one may need to use higher-order methods to accurately resolve them. Among high-order numerical methods, weighted essentially non-oscillatory (WENO) schemes, originally introduced in [29], have become one of the most widely used approaches. However, a well-known drawback of high-order WENO schemes is the high computational cost of WENO reconstructions/interpolations, which employ nonlinear weights needed to ensure stability.

One way to reduce the computational cost is to construct adaptive schemes that employ WENO reconstructions/interpolations only in regions where the solution is “rough”, while adopting some unlimited discretization elsewhere. Such an adaptive approach was introduced, for example, in [7]; see also [14, 16, 53, 55]. A key component of adaptive schemes is the design of an accurate, robust, and efficient smoothness indicator (SI) that automatically detects “rough” parts of the computed solution. A variety of SIs have been developed. Some of the SIs are based on data analyses that help measure the smoothness of the computed solution; see, e.g., [6, 17, 21, 22, 40, 43, 50, 52, 53]. There are also SIs, which measure the residual and thus check how well the computed solution satisfies the studied system of PDEs; see, e.g., [15, 26, 31, 32, 34, 42]. Another SI, introduced in [7], is based on a time-Taylor expansion applied to the computed solutions at each stage of the Runge-Kutta time integrator. In this paper, we propose an alternative approach to designing SIs based on two numerical solutions evolved simultaneously within the DF framework recently introduced in [2]; see also [1, 3, 5, 19, 41].

We focus on numerical schemes that employ two formulations of the same governing equations, namely the conservative and nonconservative (primitive) forms. To this end, we rewrite (1.1) as an equivalent (for smooth solutions) nonconservative system

$$\mathbf{V}_t + \tilde{\mathbf{F}}(\mathbf{V})_x + \tilde{\mathbf{G}}(\mathbf{V})_y = B(\mathbf{V})\mathbf{V}_x + C(\mathbf{V})\mathbf{V}_y. \quad (1.2)$$

where  $\mathbf{V} \in \mathbb{R}^d$  is the vector of primitive variables,  $\tilde{\mathbf{F}}(\mathbf{V}) : \mathbb{R}^d \rightarrow \mathbb{R}^d$  and  $\tilde{\mathbf{G}}(\mathbf{V}) : \mathbb{R}^d \rightarrow \mathbb{R}^d$  are nonlinear flux functions, and  $B(\mathbf{V}), C(\mathbf{V}) \in \mathbb{R}^{d \times d}$  are matrices characterizing the nonconservative products. As a representative example, one may consider the Euler equations of gas dynamics, which can be expressed in the form (1.1) with

$$\begin{aligned} \mathbf{U} &= (\rho, \rho u, \rho v, E)^\top, \\ \mathbf{F}(\mathbf{U}) &= (\rho u, \rho u^2 + p, \rho u v, (E + p)u)^\top, \quad \mathbf{G}(\mathbf{U}) = (\rho v, \rho u v, \rho v^2 + p, (E + p)v)^\top, \end{aligned} \quad (1.3)$$

where  $\rho$  denotes the density,  $u$  and  $v$  are the velocities in the  $x$ - and  $y$ -directions, respectively,  $p$  is the pressure, and  $E$  stands for the total energy. The system (1.1), (1.3) is completed using the equation of state, which in the ideal gas case reads as

$$E = \frac{p}{\gamma - 1} + \frac{\rho}{2}(u^2 + v^2), \quad (1.4)$$

where  $\gamma$  is the specific heat ratio. This system can be reformulated as (1.2) with

$$\begin{aligned} \mathbf{V} &= (\rho, u, v, p)^\top, \quad \tilde{\mathbf{F}}(\mathbf{V}) = \left( \rho u, \frac{u^2}{2}, 0, pu \right)^\top, \quad \tilde{\mathbf{G}}(\mathbf{V}) = \left( \rho v, 0, \frac{v^2}{2}, pv \right)^\top, \\ B(\mathbf{V}) &= \begin{pmatrix} 0 & 0 & 0 & 0 \\ 0 & 0 & 0 & -\frac{1}{\rho} \\ 0 & 0 & -u & 0 \\ 0 & -(\gamma - 1)p & 0 & 0 \end{pmatrix}, \quad C(\mathbf{V}) = \begin{pmatrix} 0 & 0 & 0 & 0 \\ 0 & -v & 0 & 0 \\ 0 & 0 & 0 & -\frac{1}{\rho} \\ 0 & 0 & -(\gamma - 1)p & 0 \end{pmatrix}. \end{aligned} \quad (1.5)$$

In the proposed adaptive DF methods, the solution is advanced in time as follows. At a given time level, we assume that we have both the computed solution and the corresponding SI values, which enable us to classify different regions of the solution as “rough” or smooth. We then advance the solution to the next time level by solving both the  $\mathbf{U}$ - and  $\mathbf{V}$ -systems, (1.1) and (1.2), respectively. This yields two approximations of the solution that are expected to differ only by truncation errors in smooth regions, but exhibit significant discrepancies in nonsmooth regions, since nonconservative schemes generally converge to incorrect solutions in the presence of discontinuities; see, e.g., [4]. Motivated by this observation, we design a new SI based on the difference between these two solutions.

We implement this SI for the Euler equations of gas dynamics. Specifically, we first consider differences in the momentum field to identify the “rough” regions, and then further examine differences in the pressure field to distinguish contact waves from the remaining “rough” areas, exploiting the fact that the pressure remains continuous across contact discontinuities.

Our adaptive strategy for solving the  $\mathbf{U}$ -system employs different numerical methods depending on the local flow features. In neighborhoods of contact waves, we follow [9] and use the second-order low-dissipation central-upwind (LDCU) scheme proposed in [11], which incorporates the overcompressive limiter of [37]. In the remaining nonsmooth regions, we apply the fifth-order alternative weighted essentially non-oscillatory (A-WENO) scheme introduced in [12]. A-WENO schemes, originally proposed in [30] (see also [12, 20, 39]), can be combined with arbitrary finite-volume numerical fluxes and WENO-type interpolations. Specifically, we use the central-upwind (CU) numerical flux from [33] together with the Ai-WENO-Z interpolation from [49]. In smooth regions, we again employ the fifth-order A-WENO scheme with the CU numerical flux, but replace the nonlinear interpolation by an unlimited one.

The  $\mathbf{V}$ -system is integrated using a simplified version of the fifth-order A-WENO scheme from [10]. It is important to emphasize that the  $\mathbf{V}$ -system solution is nonphysical and is used solely for the construction of the new SI. Therefore, once the SI values are computed, we overwrite the nonconservative  $\mathbf{V}$ -solution with the physically relevant conservative  $\mathbf{U}$ -solution before proceeding to the next time step.

The rest of the paper is organized as follows. In §2, we introduce the general idea behind the proposed approach. Our specific applications to the one-dimensional (1-D) and 2-D compressible Euler equations are described in §3 and §4, respectively. The thorough numerical validation of the approach is presented in §5. Finally, §6 outlines conclusions and further perspectives.

## 2 New Adaptive Schemes within the DF Framework

We begin with a description of the general idea by considering a 2-D hyperbolic system of conservation laws (1.1), which admits a nonconservative formulation (1.2).

We introduce a uniform Cartesian mesh consisting of nonoverlapping cells  $I_{j,k} = [x_{j-\frac{1}{2}}, x_{j+\frac{1}{2}}] \times [y_{k-\frac{1}{2}}, y_{k+\frac{1}{2}}]$  of size  $\Delta x \Delta y$  with  $x_{j+\frac{1}{2}} - x_{j-\frac{1}{2}} \equiv \Delta x$  and  $y_{k+\frac{1}{2}} - y_{k-\frac{1}{2}} \equiv \Delta y$ , centered at  $(x_j, y_k)$  with  $x_j = \frac{1}{2}(x_{j-\frac{1}{2}} + x_{j+\frac{1}{2}})$  and  $y_k = \frac{1}{2}(y_{k-\frac{1}{2}} + y_{k+\frac{1}{2}})$ , for  $j = 1, \dots, N$  and  $k = 1, \dots, M$ . We denote by  $\underline{\mathbf{U}}_{j,k}(t) \approx \mathbf{U}(x_j, y_k, t)$  the point values of  $\mathbf{U}$  computed at time  $t$ . These point values will be evolved in time using a one-step method, for which the solution update from the time level  $t^n$  to the next time level  $t^{n+1} := t^n + \Delta t$  can be, in general, written as

$$\underline{\mathbf{U}}^{n+1} = \mathcal{C}(\underline{\mathbf{U}}^n, \underline{\mathcal{E}}^n). \quad (2.1)$$

Here,  $\underline{\mathbf{U}}^n := \{\underline{\mathbf{U}}_{j,k}^n\}$  and  $\mathcal{C}(\cdot, \cdot)$  is a high-order nonlinear conservative and consistent operator with an adaptive nature, which depends on the second argument  $\underline{\mathcal{E}}^n := \{\underline{\mathcal{E}}_{j,k}^n\}$  with  $\underline{\mathcal{E}}_{j,k}^n$  representing an SI for the solution in the cell  $I_{j,k}$ .

According to  $\underline{\mathcal{E}}^n$ , we distinguish between smooth (S) and “rough” (R) areas, and within the latter one, we make a further distinction between the neighborhoods of contact discontinuities (RC) and the remaining “rough” non-contact areas (RNC). In each of these areas, we adopt a different suitable discretization as described below:

- In **Region S**, we achieve high accuracy by evolving the solution using the fifth-order A-WENO scheme based on the CU numerical fluxes and unlimited interpolation;
- In **Region RNC**, we use the same fifth-order A-WENO scheme but, in order to guarantee a robust handling of discontinuities avoiding spurious oscillations, we replace the unlimited interpolation with a local characteristic decomposition (LCD)-based fifth-order Ai-WENO-Z interpolation;
- In **Region RC**, we switch to the second-order LDCU scheme and employ an overcompressive limiter applied to the local characteristic variables in order to sharply capture linearly degenerate contact waves.

**Remark 2.1.** *It is well-known that the numerical treatment of contact discontinuities is particularly challenging. In contrast to shocks, which are supported by a self-stabilizing mechanism due to the convergence of characteristic curves and the resulting compression, linearly degenerate contact discontinuities are inevitably smeared by the numerical dissipation present in any stable numerical scheme. Despite being formally second-order accurate, the discretization employed in Region RC is well-suited for handling contact discontinuities. In fact, the LDCU numerical flux is designed to accurately capture contact discontinuities and, when combined with the overcompressive limiter, the resulting scheme is able to provide a very sharp resolution of discontinuous contact profiles. We stress, however, that overcompressive limiters must be employed in a careful way, as their use in smooth regions typically leads to the generation of artificial structures that contain kinks or spurious discontinuities.*

The SI  $\underline{\mathcal{E}}^n$  plays a crucial role in the proposed algorithm, and it is designed following ideas introduced in [8]. For this purpose, we define the point values as approximations of the primitive variables  $\mathbf{V}_{j,k}(t) := \mathbf{V}(\mathbf{U}_{j,k}(t))$ , with  $\mathbf{V}(\cdot)$  representing the transformation from the conserved to primitive variables, the vector  $\underline{\mathbf{V}}^n := \{\mathbf{V}_{j,k}^n\}$  with  $\mathbf{V}_{j,k}^n := \mathbf{V}(\mathbf{U}_{j,k}^n)$ , and we complement (2.1) with the following nonconservative update:

$$\underline{\mathbf{V}}^* = \mathcal{N}(\underline{\mathbf{U}}^n, \underline{\mathbf{V}}^n), \quad (2.2)$$

where  $\mathcal{N}(\cdot, \cdot)$  is a nonlinear high-order consistent operator.

It is well-known that nonconservative schemes tend to converge to wrong weak solutions in the presence of discontinuities; see [4, 28]. Therefore, the difference between  $\mathbf{U}_{j,k}^{n+1}$  and  $\mathbf{U}(\mathbf{V}_{j,k}^*)$ , where  $\mathbf{U}(\cdot)$  represents the transformation from the primitive to conserved variables, is expected to be consistent with the order of the scheme in the smooth areas only, while being  $\mathcal{O}(1)$  in the “rough” areas. It is therefore natural to define the components of  $\mathbf{E}^{n+1}$  as functions of the differences  $\boldsymbol{\alpha}(\mathbf{U}_{j,k}^{n+1}) - \boldsymbol{\alpha}(\mathbf{U}(\mathbf{V}_{j,k}^*))$  with  $\boldsymbol{\alpha}(\cdot)$  being a vector of quantities of interest obtained from the conserved variables. We emphasize that the updated values  $\mathbf{V}^*$  are, in general, unreliable and thus they are only used in the computation of the SI. Therefore, any linearly stable high-order scheme can be used in (2.2). Our particular choice is a simplified version of the A-WENO scheme from [10], which will be described below.

### 3 Application to the One-Dimensional Euler Equations

In this section, we apply the new adaptive scheme to the one-dimensional (1-D) Euler equations of gas dynamics, which read as

$$\begin{aligned} \mathbf{U}_t + \mathbf{F}(\mathbf{U})_x &= \mathbf{0}, \\ \mathbf{U} = (\rho, \rho u, E)^\top, \quad \mathbf{F}(\mathbf{U}) &= (\rho u, \rho u^2 + p, u(E + p))^\top, \quad E = \frac{p}{\gamma - 1} + \frac{\rho u^2}{2}. \end{aligned} \quad (3.1)$$

The primitive formulation of (3.1) reads as

$$\begin{aligned} \mathbf{V}_t + \tilde{\mathbf{F}}(\mathbf{V})_x &= B(\mathbf{V})\mathbf{V}_x, \quad \mathbf{V} = \begin{pmatrix} \rho \\ u \\ p \end{pmatrix}, \quad \tilde{\mathbf{F}}(\mathbf{V}) = \begin{pmatrix} \rho u \\ u^2/2 \\ pu \end{pmatrix}, \\ B(\mathbf{V}) &= \begin{pmatrix} 0 & 0 & 0 \\ 0 & 0 & -1/\rho \\ 0 & -(\gamma - 1)p & 0 \end{pmatrix}. \end{aligned} \quad (3.2)$$

This system can be rewritten in the following quasi-conservative form:

$$\mathbf{V}_t + \mathbf{K}_x = \mathbf{0}, \quad \mathbf{K} := \tilde{\mathbf{F}}(\mathbf{V}) - \mathbf{R}, \quad \mathbf{R} := \int_{\hat{x}}^x B(\mathbf{V})\mathbf{V}_\xi(\xi, t) d\xi, \quad (3.3)$$

where  $\mathbf{K}$  is a global flux and  $\hat{x}$  is an arbitrary number.

We introduce a uniform mesh consisting of the cells  $I_j = [x_{j-\frac{1}{2}}, x_{j+\frac{1}{2}}]$  of size  $x_{j+\frac{1}{2}} - x_{j-\frac{1}{2}} \equiv \Delta x$  with centers  $x_j = \frac{1}{2}(x_{j-\frac{1}{2}} + x_{j+\frac{1}{2}})$ , for  $j = 1, \dots, N$ . We denote by  $\mathbf{U}_j(t) \approx \mathbf{U}(x_j, t)$  and  $\mathbf{V}_j(t) := \mathbf{V}(\mathbf{U}_j(t))$ , and assume that at time level  $t^n$  the solution, realized in terms of  $\mathbf{U}_j^n := \mathbf{U}_j(t^n)$  and  $\mathbf{V}_j^n := \mathbf{V}_j(t^n)$ , is available. Within the time interval  $[t^n, t^{n+1}]$ , the solution is evolved according to the following semi-discretizations of the conservative  $\mathbf{U}$ -system (3.1) and nonconservative  $\mathbf{V}$ -system (3.2):

$$\frac{d}{dt} \mathbf{U}_j(t) = -\frac{\mathcal{F}_{j+\frac{1}{2}}(t) - \mathcal{F}_{j-\frac{1}{2}}(t)}{\Delta x}, \quad (3.4)$$

$$\frac{d}{dt} \mathbf{V}_j(t) = -\frac{\mathcal{K}_{j+\frac{1}{2}}(t) - \mathcal{K}_{j-\frac{1}{2}}(t)}{\Delta x}, \quad (3.5)$$

where  $\mathcal{F}_{j+\frac{1}{2}}$  and  $\mathcal{K}_{j+\frac{1}{2}}$  are the corresponding numerical fluxes, which will be described below.

Notice that most of the indexed quantities are time-dependent, but from now on, we will omit this dependence for the sake of brevity.

### 3.1 Adaptive Criteria

For the 1-D Euler equations, we denote  $\boldsymbol{\varepsilon} := (\varepsilon^{\rho u}, \varepsilon^p)^\top$  and define the grid values of  $\varepsilon^{\rho u}$  and  $\varepsilon^p$  as

$$\varepsilon_j^{\rho u} := [\alpha^{\rho u}(\mathbf{U}_j) - \alpha^{\rho u}(\mathbf{U}(\mathbf{V}_j^*))]^2, \quad \varepsilon_j^p := [\alpha^p(\mathbf{U}_j) - \alpha^p(\mathbf{U}(\mathbf{V}_j^*))]^2,$$

where we select  $\boldsymbol{\alpha} = (\alpha^{\rho u}, \alpha^p)^\top := (\rho u, p)^\top$ . We then smooth out these quantities by introducing

$$\begin{aligned} (\overline{\varepsilon^{\rho u}})_j &= \frac{\varepsilon_{j-2}^{\rho u} + 4\varepsilon_{j-1}^{\rho u} + 8\varepsilon_j^{\rho u} + 4\varepsilon_{j+1}^{\rho u} + \varepsilon_{j+2}^{\rho u}}{18}, \\ (\overline{\varepsilon^p})_j &= \frac{\varepsilon_{j-2}^p + 4\varepsilon_{j-1}^p + 8\varepsilon_j^p + 4\varepsilon_{j+1}^p + \varepsilon_{j+2}^p}{18}, \end{aligned}$$

take their averages over the entire computational domain:

$$(\overline{\varepsilon^{\rho u}})_{\text{ave}} := \frac{1}{N} \sum_{j=1}^N (\overline{\varepsilon^{\rho u}})_j, \quad (\overline{\varepsilon^p})_{\text{ave}} := \frac{1}{N} \sum_{j=1}^N (\overline{\varepsilon^p})_j,$$

and define the following quantities at the cell interfaces:

$$\varepsilon_{j+\frac{1}{2}}^{\rho u} := \max \{(\overline{\varepsilon^{\rho u}})_j, (\overline{\varepsilon^{\rho u}})_{j+1}\}, \quad \varepsilon_{j+\frac{1}{2}}^p := \max \{(\overline{\varepsilon^p})_j, (\overline{\varepsilon^p})_{j+1}\}.$$

We now select Regions S, RNC, and RC based on the consideration that while in the smooth regions both  $\varepsilon_{j+\frac{1}{2}}^{\rho u}$  and  $\varepsilon_{j+\frac{1}{2}}^p$  are supposed to be very small,  $\varepsilon_{j+\frac{1}{2}}^{\rho u}$  is expected to be  $\mathcal{O}(1)$  near both shocks and contact discontinuities, while  $\varepsilon_{j+\frac{1}{2}}^p$  is expected to be  $\mathcal{O}(1)$  near the shocks only as  $p$  stays continuous across the contact discontinuities. In particular, the selection is carried out as follows:

$$x_{j+\frac{1}{2}} \in \begin{cases} \text{Region S,} & \text{if } \varepsilon_{j+\frac{1}{2}}^{\rho u} < \kappa_{\rho u} (\overline{\varepsilon^{\rho u}})_{\text{ave}}, \\ \text{Region RC,} & \text{if } \varepsilon_{j+\frac{1}{2}}^{\rho u} > \kappa_{\rho u} (\overline{\varepsilon^{\rho u}})_{\text{ave}} \text{ and } \varepsilon_{j+\frac{1}{2}}^p < \kappa_p (\overline{\varepsilon^p})_{\text{ave}}, \\ \text{Region RNC,} & \text{if } \varepsilon_{j+\frac{1}{2}}^{\rho u} > \kappa_{\rho u} (\overline{\varepsilon^{\rho u}})_{\text{ave}} \text{ and } \varepsilon_{j+\frac{1}{2}}^p > \kappa_p (\overline{\varepsilon^p})_{\text{ave}}, \end{cases}$$

where  $\kappa_{\rho u}$  and  $\kappa_p$  are two test-dependent adaption coefficients to be tuned.

### 3.2 Numerical Solvers for the Conservative System

We use the semi-discretization (3.4) with numerical fluxes  $\mathcal{F}_{j+\frac{1}{2}}$ , which are obtained out of the finite-volume fluxes  $\mathcal{F}_{j+\frac{1}{2}}^{\text{FV}} := \mathcal{F}^{\text{FV}}(\mathbf{U}_{j+\frac{1}{2}}^-, \mathbf{U}_{j+\frac{1}{2}}^+)$ , where  $\mathbf{U}_{j+\frac{1}{2}}^\pm$  are point values at the cell interface  $x_{j+\frac{1}{2}}$ , obtained adaptively using a proper interpolation/reconstruction.

In particular, given the reconstructed/interpolated values at each cell interface (we will describe later how to obtain them), we first compute the finite-volume numerical fluxes  $\mathcal{F}_{j+\frac{1}{2}}^{\text{FV}}$  as follows: if  $x_{j+\frac{1}{2}}$  is in

either Regions S or RNC,  $\mathcal{F}_{j+\frac{1}{2}}^{\text{FV}}$  is the CU numerical flux from [33], while, if  $x_{j+\frac{1}{2}}$  is in Region RC,  $\mathcal{F}_{j+\frac{1}{2}}^{\text{FV}}$  is the LDCU numerical flux from [11].

We then proceed with computing the numerical fluxes  $\mathcal{F}_{j+\frac{1}{2}}$ . If  $x_{j+\frac{1}{2}}$  is in either Regions S or RNC, we use the fifth-order A-WENO numerical flux from [12], which reads as

$$\mathcal{F}_{j+\frac{1}{2}} = \mathcal{F}_{j+\frac{1}{2}}^{\text{FV}} - \frac{1}{24}(\Delta x)^2(\mathbf{F}_{xx})_{j+\frac{1}{2}} + \frac{7}{5760}(\Delta x)^4(\mathbf{F}_{xxxx})_{j+\frac{1}{2}}, \quad (3.6)$$

where the high-order correction terms are computed through central differences

$$\begin{aligned} (\mathbf{F}_{xx})_{j+\frac{1}{2}} &= \frac{-\mathcal{F}_{j-\frac{3}{2}}^{\text{FV}} + 16\mathcal{F}_{j-\frac{1}{2}}^{\text{FV}} - 30\mathcal{F}_{j+\frac{1}{2}}^{\text{FV}} + 16\mathcal{F}_{j+\frac{3}{2}}^{\text{FV}} - \mathcal{F}_{j+\frac{5}{2}}^{\text{FV}}}{12(\Delta x)^2}, \\ (\mathbf{F}_{xxxx})_{j+\frac{1}{2}} &= \frac{\mathcal{F}_{j-\frac{3}{2}}^{\text{FV}} - 4\mathcal{F}_{j-\frac{1}{2}}^{\text{FV}} + 6\mathcal{F}_{j+\frac{1}{2}}^{\text{FV}} - 4\mathcal{F}_{j+\frac{3}{2}}^{\text{FV}} + \mathcal{F}_{j+\frac{5}{2}}^{\text{FV}}}{(\Delta x)^4}, \end{aligned} \quad (3.7)$$

applied to the already computed finite-volume numerical fluxes. If  $x_{j+\frac{1}{2}}$  is in Region RC, we set  $\mathcal{F}_{j+\frac{1}{2}} = \mathcal{F}_{j+\frac{1}{2}}^{\text{FV}}$  to fully exploit the ability of the second-order LDCU scheme to capture contact discontinuities.

**Remark 3.1.** *We do not provide details on the CU and LDCU numerical fluxes for the sake of brevity.*

We compute the point values  $\mathbf{U}_{j+\frac{1}{2}}^\pm$  as follows. If  $x_{j+\frac{1}{2}} \in$  Region S, we use the fourth-degree polynomials and compute the fifth-order interpolants over the stencils  $\{x_{j-2}, x_{j-1}, x_j, x_{j+1}, x_{j+2}\}$  and  $\{x_{j-1}, x_j, x_{j+1}, x_{j+2}, x_{j+3}\}$  to obtain

$$\mathbf{U}_{j+\frac{1}{2}}^- = \frac{3\mathbf{U}_{j-2} - 20\mathbf{U}_{j-1} + 90\mathbf{U}_j + 60\mathbf{U}_{j+1} - 5\mathbf{U}_{j+2}}{128}, \quad (3.8)$$

and

$$\mathbf{U}_{j+\frac{1}{2}}^+ = \frac{-5\mathbf{U}_{j-1} + 60\mathbf{U}_j + 90\mathbf{U}_{j+1} - 20\mathbf{U}_{j+2} + 3\mathbf{U}_{j+3}}{128}, \quad (3.9)$$

respectively.

In “rough” regions, in order to minimize spurious oscillations, which can be triggered by the use of either a high-order interpolation or an overcompressive limiter, we perform the interpolation/reconstruction in the local characteristic variables  $\boldsymbol{\Gamma}$ , which are obtained using the LCD. To this end, we first compute averaged values  $\widehat{\mathbf{U}}_{j+\frac{1}{2}}$  (in the numerical examples presented in §5, we have used the Roe averages, and define the local linearized Jacobians  $\widehat{\mathbf{A}}_{j+\frac{1}{2}} := \frac{\partial \mathbf{F}}{\partial \mathbf{U}}(\widehat{\mathbf{U}}_{j+\frac{1}{2}})$ . These matrices can be diagonalized using the matrices of their eigenvectors,  $\mathbf{R}_{j+\frac{1}{2}}$ , so that  $\mathbf{R}_{j+\frac{1}{2}}^{-1} \widehat{\mathbf{A}}_{j+\frac{1}{2}} \mathbf{R}_{j+\frac{1}{2}}$  are diagonal matrices. We then introduce the local characteristic variables in the neighborhood of  $x = x_{j+\frac{1}{2}}$ ,

$$\boldsymbol{\Gamma}_\ell := \mathbf{R}_{j+\frac{1}{2}}^{-1} \mathbf{U}_\ell, \quad \ell = j-2, \dots, j+3, \quad (3.10)$$

and distinguish between the two different “rough” regions.

- If  $x_{j+\frac{1}{2}} \in$  Region RNC, we use the values  $\boldsymbol{\Gamma}_\ell$  in (3.10) to compute the point values  $\boldsymbol{\Gamma}_{j+\frac{1}{2}}^\pm$  with the help of the fifth-order Ai-WENO-Z interpolation, whose detailed description can be found in [18, §2.2].

- If  $x_{j+\frac{1}{2}} \in$  Region RC, we employ the overcompressive limiter to evaluate the slopes

$$\begin{aligned} (\boldsymbol{\Gamma}_x)_j &= \phi_{\theta, \tau}^{\text{SBM}} \left( \frac{\boldsymbol{\Gamma}_{j+1} - \boldsymbol{\Gamma}_j}{\boldsymbol{\Gamma}_j - \boldsymbol{\Gamma}_{j-1}} \right) \frac{\boldsymbol{\Gamma}_j - \boldsymbol{\Gamma}_{j-1}}{\Delta x}, \\ (\boldsymbol{\Gamma}_x)_{j+1} &= \phi_{\theta, \tau}^{\text{SBM}} \left( \frac{\boldsymbol{\Gamma}_{j+2} - \boldsymbol{\Gamma}_{j+1}}{\boldsymbol{\Gamma}_{j+1} - \boldsymbol{\Gamma}_j} \right) \frac{\boldsymbol{\Gamma}_{j+1} - \boldsymbol{\Gamma}_j}{\Delta x}, \end{aligned} \quad (3.11)$$

where the two-parameter SBM function

$$\phi_{\theta, \tau}^{\text{SBM}}(r) := \begin{cases} 0 & \text{if } r < 0, \\ \min\{r\theta, 1 + \tau(r - 1)\} & \text{if } 0 < r \leq 1, \\ r\phi_{\theta, \tau}^{\text{SBM}}(1/r) & \text{otherwise,} \end{cases} \quad (3.12)$$

is applied in the component-wise manner. We set  $\theta = 2$  and  $\tau = -0.25$ , which correspond to the overcompressive regime; see [37]. Equipped with (3.11), we evaluate

$$\boldsymbol{\Gamma}_{j+\frac{1}{2}}^- = \boldsymbol{\Gamma}_j + \frac{\Delta x}{2}(\boldsymbol{\Gamma}_x)_j \quad \text{and} \quad \boldsymbol{\Gamma}_{j+\frac{1}{2}}^+ = \boldsymbol{\Gamma}_{j+1} - \frac{\Delta x}{2}(\boldsymbol{\Gamma}_x)_{j+1}.$$

Finally, in both Regions RNC and RC, we obtain the corresponding point values of  $\boldsymbol{U}$  by

$$\boldsymbol{U}_{j+\frac{1}{2}}^\pm = R_{j+\frac{1}{2}} \boldsymbol{\Gamma}_{j+\frac{1}{2}}^\pm.$$

### 3.3 Numerical Solver for the Primitive System

We employ the semi-discretization (3.5) with the fifth-order global numerical fluxes

$$\mathcal{K}_{j+\frac{1}{2}} = \mathcal{K}_{j+\frac{1}{2}}^{\text{FV}} - \frac{1}{24}(\Delta x)^2(\boldsymbol{K}_{xx})_{j+\frac{1}{2}} + \frac{7}{5760}(\Delta x)^4(\boldsymbol{K}_{xxxx})_{j+\frac{1}{2}}, \quad (3.13)$$

where  $\mathcal{K}_{j+\frac{1}{2}}^{\text{FV}}$  is a simplified version of the finite-volume PCCU numerical global flux from [13] and the high-order correction terms are computed the same way as in (3.6)–(3.7), namely,

$$\begin{aligned} (\boldsymbol{K}_{xx})_{j+\frac{1}{2}} &= \frac{-\mathcal{K}_{j-\frac{3}{2}}^{\text{FV}} + 16\mathcal{K}_{j-\frac{1}{2}}^{\text{FV}} - 30\mathcal{K}_{j+\frac{1}{2}}^{\text{FV}} + 16\mathcal{K}_{j+\frac{3}{2}}^{\text{FV}} - \mathcal{K}_{j+\frac{5}{2}}^{\text{FV}}}{12(\Delta x)^2}, \\ (\boldsymbol{K}_{xxxx})_{j+\frac{1}{2}} &= \frac{\mathcal{K}_{j-\frac{3}{2}}^{\text{FV}} - 4\mathcal{K}_{j-\frac{1}{2}}^{\text{FV}} + 6\mathcal{K}_{j+\frac{1}{2}}^{\text{FV}} - 4\mathcal{K}_{j+\frac{3}{2}}^{\text{FV}} + \mathcal{K}_{j+\frac{5}{2}}^{\text{FV}}}{(\Delta x)^4}. \end{aligned} \quad (3.14)$$

The finite-volume numerical global fluxes are given by

$$\mathcal{K}_{j+\frac{1}{2}}^{\text{FV}} = \frac{a_{j+\frac{1}{2}}^+ \boldsymbol{K}_{j+\frac{1}{2}}^- - a_{j+\frac{1}{2}}^- \boldsymbol{K}_{j+\frac{1}{2}}^+}{a_{j+\frac{1}{2}}^+ - a_{j+\frac{1}{2}}^-} + \frac{a_{j+\frac{1}{2}}^+ a_{j+\frac{1}{2}}^-}{a_{j+\frac{1}{2}}^+ - a_{j+\frac{1}{2}}^-} \left( \boldsymbol{V}_{j+\frac{1}{2}}^+ - \boldsymbol{V}_{j+\frac{1}{2}}^- \right), \quad (3.15)$$

where  $\boldsymbol{V}_{j+\frac{1}{2}}^\pm$  are one-sided cell interface point values. We stress that our goal is to enforce the linear stability of the primitive system solver, and hence  $\boldsymbol{V}_{j+\frac{1}{2}}^\pm$  are obtained using the same fifth-order unlimited

interpolation as in (3.8)–(3.9), which gives

$$\begin{aligned}\mathbf{V}_{j+\frac{1}{2}}^- &= \frac{3\mathbf{V}_{j-2} - 20\mathbf{V}_{j-1} + 90\mathbf{V}_j + 60\mathbf{V}_{j+1} - 5\mathbf{V}_{j+2}}{128}, \\ \mathbf{V}_{j+\frac{1}{2}}^+ &= \frac{-5\mathbf{V}_{j-1} + 60\mathbf{V}_j + 90\mathbf{V}_{j+1} - 20\mathbf{V}_{j+2} + 3\mathbf{V}_{j+3}}{128}.\end{aligned}$$

In (3.15),  $a_{j+\frac{1}{2}}^\pm$  are the one-sided local speeds of propagation estimated by

$$\begin{aligned}a_{j+\frac{1}{2}}^+ &= \max \left\{ u_{j+\frac{1}{2}}^- + c_{j+\frac{1}{2}}^-, u_{j+\frac{1}{2}}^+ + c_{j+\frac{1}{2}}^+, \delta \right\}, \\ a_{j+\frac{1}{2}}^- &= \min \left\{ u_{j+\frac{1}{2}}^- - c_{j+\frac{1}{2}}^-, u_{j+\frac{1}{2}}^+ - c_{j+\frac{1}{2}}^+, -\delta \right\},\end{aligned}\tag{3.16}$$

where  $c := \sqrt{\gamma p / \rho}$  is the speed of sound,  $u_{j+\frac{1}{2}}^\pm$  and  $c_{j+\frac{1}{2}}^\pm$  are computed from  $\mathbf{V}_{j+\frac{1}{2}}^\pm$ , and  $\delta = 10^{-10}$  is a small constant needed to prevent division by zero.

A simplification compared with the numerical global flux from [13] is in the evaluation of  $\mathbf{K}_{j+\frac{1}{2}}^\pm$ , which is now conducted by neglecting a special path-conservative treatment of the interface jump associated with the nonconservative product terms. Namely, we set

$$\mathbf{K}_{j+\frac{1}{2}}^\pm = \tilde{\mathbf{F}}(\mathbf{V}_{j+\frac{1}{2}}^\pm) - \mathbf{R}_{j+\frac{1}{2}},\tag{3.17}$$

where the global part of the numerical flux is evaluated recursively as follows. First, we set  $\hat{x} = x_{\frac{1}{2}}$  so that  $\mathbf{R}_{\frac{1}{2}} = \mathbf{0}$ , and then we compute

$$\mathbf{R}_{j+\frac{1}{2}} = \mathbf{R}_{j-\frac{1}{2}} + \mathbf{B}_j, \quad j = 1, \dots, N,\tag{3.18}$$

where  $\mathbf{B}_j$  is a fifth-order approximation of the integral of the nonconservative product terms over the cell  $I_j$ :

$$\mathbf{B}_j \approx \int_{I_{j+\frac{1}{2}}} B(\mathbf{V}) \mathbf{V}_x \, dx.\tag{3.19}$$

To evaluate these integrals, we use the fifth-order Newton-Cotes quadrature with the nodes  $x_{j-\frac{1}{2}}, x_{j-\frac{1}{4}}, x_j, x_{j+\frac{1}{4}}, x_{j+\frac{1}{2}}$ ; see [18, Appendix A] for details. When this quadrature is applied, one needs to interpolate the values  $\mathbf{V}_{j\pm\frac{1}{4}}$  at the points  $x = x_{j\pm\frac{1}{4}}$ . This is done with the help of the fifth-order (fourth-degree) polynomial interpolant over the stencil  $\{x_{j-2}, x_{j-1}, x_j, x_{j+1}, x_{j+2}\}$ , which gives

$$\begin{aligned}\mathbf{V}_{j-\frac{1}{4}} &= \frac{-45\mathbf{V}_{j-2} + 420\mathbf{V}_{j-1} + 1890\mathbf{V}_j - 252\mathbf{V}_{j+1} + 35\mathbf{V}_{j+2}}{2048}, \\ \mathbf{V}_{j+\frac{1}{4}} &= \frac{35\mathbf{V}_{j-2} - 252\mathbf{V}_{j-1} + 1890\mathbf{V}_j + 420\mathbf{V}_{j+1} - 45\mathbf{V}_{j+2}}{2048}.\end{aligned}$$

**Remark 3.2.** *We stress again that the solution  $\underline{\mathbf{V}}^*$ , obtained upon completion of one time evolution step according to the simplified and only linearly stable semi-discrete scheme (3.5), (3.13)–(3.19), will be accurate in the smooth regions only, while it may contain severe oscillations near the discontinuities. This behavior is not only acceptable, but, in fact, advantageous since the solution  $\underline{\mathbf{V}}^*$  is used exclusively to compute the SI and thus to detect Regions S, RC, and RNC.*

## 4 Application to the Two-Dimensional Euler Equations

In this section, we apply the new adaptive scheme to the 2-D Euler equations of gas dynamics, whose conservative and primitive formulations are given by (1.1), (1.3)–(1.4) and (1.2), (1.5), respectively. As in the 1-D case, the primitive system can be rewritten in the quasi-conservative form as

$$\begin{aligned} \mathbf{V}_t + \mathbf{K}_x + \mathbf{L}_y &= \mathbf{0}, \quad \mathbf{K} = \tilde{\mathbf{F}}(\mathbf{V}) - \mathbf{R}, \quad \mathbf{L} = \tilde{\mathbf{G}}(\mathbf{V}) - \mathbf{S}, \\ \mathbf{R} &:= \int_{\hat{x}}^x B(\mathbf{V}) \mathbf{V}_\xi(\xi, y, t) d\xi, \quad \mathbf{S} := \int_{\hat{y}}^y C(\mathbf{V}) \mathbf{V}_\eta(x, \eta, t) d\eta, \end{aligned} \quad (4.1)$$

where  $\mathbf{K}$  and  $\mathbf{L}$  are global fluxes and  $\hat{x}$  and  $\hat{y}$  are arbitrary numbers.

Within the time interval  $[t^n, t^{n+1}]$ , the solution is evolved according to the following semi-discretizations of the conservative  $\mathbf{U}$ -system (1.1), (1.3)–(1.4) and nonconservative  $\mathbf{V}$ -system (1.2), (1.5):

$$\frac{d}{dt} \mathbf{U}_{j,k} = -\frac{\mathcal{F}_{j+\frac{1}{2},k} - \mathcal{F}_{j-\frac{1}{2},k}}{\Delta x} - \frac{\mathcal{G}_{j,k+\frac{1}{2}} - \mathcal{G}_{j,k-\frac{1}{2}}}{\Delta y}, \quad (4.2)$$

$$\frac{d}{dt} \mathbf{V}_{j,k} = -\frac{\mathcal{K}_{j+\frac{1}{2},k} - \mathcal{K}_{j-\frac{1}{2},k}}{\Delta x} - \frac{\mathcal{L}_{j,k+\frac{1}{2}} - \mathcal{L}_{j,k-\frac{1}{2}}}{\Delta y}, \quad (4.3)$$

where  $\mathcal{F}_{j+\frac{1}{2},k}$ ,  $\mathcal{G}_{j,k+\frac{1}{2}}$  and  $\mathcal{K}_{j+\frac{1}{2},k}$ ,  $\mathcal{L}_{j,k+\frac{1}{2}}$  are the corresponding numerical fluxes, which will be described below.

### 4.1 Adaptive Criteria

For the 2-D Euler equations, we define the grid values of  $\varepsilon^{\rho u}$ ,  $\varepsilon^{\rho v}$ , and  $\varepsilon^p$  as

$$\begin{aligned} \varepsilon_{j,k}^{\rho u} &:= [\alpha^{\rho u}(\mathbf{U}_{j,k}) - \alpha^{\rho u}(\mathbf{U}(\mathbf{V}_{j,k}^*))]^2, \quad \varepsilon_{j,k}^{\rho v} := [\alpha^{\rho v}(\mathbf{U}_{j,k}) - \alpha^{\rho v}(\mathbf{U}(\mathbf{V}_{j,k}^*))]^2, \\ \varepsilon_{j,k}^p &:= [\alpha^p(\mathbf{U}_{j,k}) - \alpha^p(\mathbf{U}(\mathbf{V}_{j,k}^*))]^2, \end{aligned}$$

and select  $\boldsymbol{\alpha} = (\alpha^{\rho u}, \alpha^{\rho v}, \alpha^p)^\top := (\rho u, \rho v, p)^\top$ , denote  $\boldsymbol{\varepsilon} := (\varepsilon^{\rho u}, \varepsilon^{\rho v}, \varepsilon^p)^\top$ , and define the grid values of  $\varepsilon^{\rho u}$ ,  $\varepsilon^{\rho v}$ , and  $\varepsilon^p$  as

In the 2-D case, we extend the adaptive criteria introduced in §3.1 in a dimension-by-dimension manner. We therefore check smoothness of the computed solution at the midpoints of the cell interfaces in each of the directions separately.

We begin with the cell interfaces in the  $x$ -direction. We first smooth out  $\varepsilon_{j,k}^{\rho u}$  and  $\varepsilon_{j,k}^p$  by introducing

$$\begin{aligned} (\overline{\varepsilon^{\rho u}})_j^x &= \frac{\varepsilon_{j-2,k}^{\rho u} + 4\varepsilon_{j-1,k}^{\rho u} + 8\varepsilon_{j,k}^{\rho u} + 4\varepsilon_{j+1,k}^{\rho u} + \varepsilon_{j+2,k}^{\rho u}}{18}, \\ (\overline{\varepsilon^p})_j^x &= \frac{\varepsilon_{j-2,k}^p + 4\varepsilon_{j-1,k}^p + 8\varepsilon_{j,k}^p + 4\varepsilon_{j+1,k}^p + \varepsilon_{j+2,k}^p}{18}, \end{aligned}$$

take their averages over the entire computational domain:

$$(\overline{\varepsilon^{\rho u}})_{\text{ave}}^x := \frac{1}{NM} \sum_{j=1}^N \sum_{k=1}^M (\overline{\varepsilon^{\rho u}})_j^x, \quad (\overline{\varepsilon^p})_{\text{ave}}^x := \frac{1}{NM} \sum_{j=1}^N \sum_{k=1}^M (\overline{\varepsilon^p})_j^x,$$

and define the following quantities at  $(x_{j+\frac{1}{2}}, y_k)$ :

$$\varepsilon_{j+\frac{1}{2},k}^{\rho u} := \max \{ (\bar{\varepsilon}^{\rho u})_{j,k}^x, (\bar{\varepsilon}^{\rho u})_{j+1,k}^x \}, \quad \varepsilon_{j+\frac{1}{2},k}^p := \max \{ (\bar{\varepsilon}^p)_{j,k}^x, (\bar{\varepsilon}^p)_{j+1,k}^x \}.$$

We then use the following simple strategy for automatically performing the classification of the  $x$ -directional interfaces:

$$(x_{j+\frac{1}{2}}, y_k) \in \begin{cases} \text{Region S,} & \text{if } \varepsilon_{j+\frac{1}{2},k}^{\rho u} < \kappa_{\rho u} (\bar{\varepsilon}^{\rho u})_{\text{ave}}^x, \\ \text{Region RC,} & \text{if } \varepsilon_{j+\frac{1}{2},k}^{\rho u} > \kappa_{\rho u} (\bar{\varepsilon}^{\rho u})_{\text{ave}}^x \text{ and } \varepsilon_{j+\frac{1}{2},k}^p < \kappa_p (\bar{\varepsilon}^p)_{\text{ave}}^x, \\ \text{Region RNC,} & \text{if } \varepsilon_{j+\frac{1}{2},k}^{\rho u} > \kappa_{\rho u} (\bar{\varepsilon}^{\rho u})_{\text{ave}}^x \text{ and } \varepsilon_{j+\frac{1}{2},k}^p > \kappa_p (\bar{\varepsilon}^p)_{\text{ave}}^x, \end{cases}$$

where  $\kappa_{\rho u}$  and  $\kappa_p$ , as before, are two test-dependent adaption coefficients to be tuned.

Next, we proceed with the cell interfaces in the  $y$ -direction in a similar manner. We first compute

$$(\bar{\varepsilon}^{\rho v})_{j,k}^y = \frac{\varepsilon_{j,k-2}^{\rho v} + 4\varepsilon_{j,k-1}^{\rho v} + 8\varepsilon_{j,k}^{\rho v} + 4\varepsilon_{j,k+1}^{\rho v} + \varepsilon_{j,k+2}^{\rho v}}{18},$$

$$(\bar{\varepsilon}^p)_{j,k}^y = \frac{\varepsilon_{j,k-2}^p + 4\varepsilon_{j,k-1}^p + 8\varepsilon_{j,k}^p + 4\varepsilon_{j,k+1}^p + \varepsilon_{j,k+2}^p}{18},$$

$$(\bar{\varepsilon}^{\rho v})_{\text{ave}}^y := \frac{1}{NM} \sum_{j=1}^N \sum_{k=1}^M (\bar{\varepsilon}^{\rho v})_{j,k}^y, \quad (\bar{\varepsilon}^p)_{\text{ave}}^y := \frac{1}{NM} \sum_{j=1}^N \sum_{k=1}^M (\bar{\varepsilon}^p)_{j,k}^y,$$

and

$$\varepsilon_{j,k+\frac{1}{2}}^{\rho v} := \max \{ (\bar{\varepsilon}^{\rho v})_{j,k}^y, (\bar{\varepsilon}^{\rho v})_{j,k+1}^y \}, \quad \varepsilon_{j,k+\frac{1}{2}}^p := \max \{ (\bar{\varepsilon}^p)_{j,k}^y, (\bar{\varepsilon}^p)_{j,k+1}^y \},$$

and then perform the classification of the  $y$ -directional interfaces:

$$(x_j, y_{k+\frac{1}{2}}) \in \begin{cases} \text{Region S,} & \text{if } \varepsilon_{j,k+\frac{1}{2}}^{\rho v} < \kappa_{\rho v} (\bar{\varepsilon}^{\rho v})_{\text{ave}}^y, \\ \text{Region RC,} & \text{if } \varepsilon_{j,k+\frac{1}{2}}^{\rho v} > \kappa_{\rho v} (\bar{\varepsilon}^{\rho v})_{\text{ave}}^y \text{ and } \varepsilon_{j,k+\frac{1}{2}}^p < \kappa_p (\bar{\varepsilon}^p)_{\text{ave}}^y, \\ \text{Region RNC,} & \text{if } \varepsilon_{j,k+\frac{1}{2}}^{\rho v} > \kappa_{\rho v} (\bar{\varepsilon}^{\rho v})_{\text{ave}}^y \text{ and } \varepsilon_{j,k+\frac{1}{2}}^p > \kappa_p (\bar{\varepsilon}^p)_{\text{ave}}^y, \end{cases}$$

where  $\kappa_{\rho v}$  and  $\kappa_p$  are two test-dependent adaption coefficients to be tuned.

## 4.2 Numerical Solvers for the Conservative System

We employ the semi-discretization (4.2) with numerical fluxes  $\mathcal{F}_{j+\frac{1}{2},k}$  and  $\mathcal{G}_{j,k+\frac{1}{2}}$ , obtained out of pre-computed second-order finite-volume ones  $\mathcal{F}_{j+\frac{1}{2},k}^{\text{FV}} := \mathcal{F}^{\text{FV}}(\mathbf{U}_{j+\frac{1}{2},k}^-, \mathbf{U}_{j+\frac{1}{2},k}^+)$  and  $\mathcal{G}_{j,k+\frac{1}{2}}^{\text{FV}} := \mathcal{G}^{\text{FV}}(\mathbf{U}_{j,k+\frac{1}{2}}^-, \mathbf{U}_{j,k+\frac{1}{2}}^+)$ , where the point values  $\mathbf{U}_{j+\frac{1}{2},k}^\pm$  and  $\mathbf{U}_{j,k+\frac{1}{2}}^\pm$  are reconstructed/interpolated on both sides at  $(x_{j+\frac{1}{2}}, y_k)$  and  $(x_j, y_{k+\frac{1}{2}})$ , respectively. These values are obtained adaptively using proper reconstruction/interpolation, as detailed later.

We first compute the finite-volume numerical fluxes  $\mathcal{F}_{j+\frac{1}{2},k}^{\text{FV}}$  in the  $x$ -direction as follows: if  $(x_{j+\frac{1}{2}}, y_k)$  is in either Regions S or RNC,  $\mathcal{F}_{j+\frac{1}{2},k}^{\text{FV}}$  is the 2-D CU numerical flux from [33], while, if  $(x_{j+\frac{1}{2}}, y_k)$  is in Region RC,  $\mathcal{F}_{j+\frac{1}{2},k}^{\text{FV}}$  is the 2-D LDCU numerical flux from [11].

We then compute the numerical fluxes  $\mathcal{F}_{j+\frac{1}{2},k}$ . If  $(x_{j+\frac{1}{2}}, y_k)$  is in either Regions S or RNC, we use the fifth-order A-WENO numerical flux from [12], which reads as

$$\mathcal{F}_{j+\frac{1}{2},k} = \mathcal{F}_{j+\frac{1}{2},k}^{\text{FV}} - \frac{1}{24}(\Delta x)^2(\mathbf{F}_{xx})_{j+\frac{1}{2},k} + \frac{7}{5760}(\Delta x)^4(\mathbf{F}_{xxxx})_{j+\frac{1}{2},k}, \quad (4.4)$$

where the high-order correction terms are computed through central differences:

$$\begin{aligned} (\mathbf{F}_{xx})_{j+\frac{1}{2},k} &= \frac{-\mathcal{F}_{j-\frac{3}{2},k}^{\text{FV}} + 16\mathcal{F}_{j-\frac{1}{2},k}^{\text{FV}} - 30\mathcal{F}_{j+\frac{1}{2},k}^{\text{FV}} + 16\mathcal{F}_{j+\frac{3}{2},k}^{\text{FV}} - \mathcal{F}_{j+\frac{5}{2},k}^{\text{FV}}}{12(\Delta x)^2}, \\ (\mathbf{F}_{xxxx})_{j+\frac{1}{2},k} &= \frac{\mathcal{F}_{j-\frac{3}{2},k}^{\text{FV}} - 4\mathcal{F}_{j-\frac{1}{2},k}^{\text{FV}} + 6\mathcal{F}_{j+\frac{1}{2},k}^{\text{FV}} - 4\mathcal{F}_{j+\frac{3}{2},k}^{\text{FV}} + \mathcal{F}_{j+\frac{5}{2},k}^{\text{FV}}}{(\Delta x)^4}. \end{aligned} \quad (4.5)$$

applied to the already computed finite-volume numerical fluxes. If  $(x_{j+\frac{1}{2}}, y_k)$  is in Region RC, we set  $\mathcal{F}_{j+\frac{1}{2},k} = \mathcal{F}_{j+\frac{1}{2},k}^{\text{FV}}$ , coinciding with the 2-D second-order LDCU numerical flux from [11].

The numerical fluxes in the  $y$ -direction are obtained similarly. We start by computing the finite-volume fluxes  $\mathcal{G}_{j,k+\frac{1}{2}}^{\text{FV}}$  as follows: if  $(x_j, y_{k+\frac{1}{2}})$  is in either Regions S or RNC,  $\mathcal{G}_{j,k+\frac{1}{2}}^{\text{FV}}$  is the 2-D CU numerical flux from [33], while, if  $(x_j, y_{k+\frac{1}{2}})$  is in Region RC,  $\mathcal{G}_{j,k+\frac{1}{2}}^{\text{FV}}$  is the 2-D LDCU numerical flux from [11].

We then compute the numerical fluxes  $\mathcal{G}_{j,k+\frac{1}{2}}$ . If  $(x_j, y_{k+\frac{1}{2}})$  is in either Regions S or RNC, we use the fifth-order A-WENO numerical flux from [12], which reads as

$$\mathcal{G}_{j,k+\frac{1}{2}} = \mathcal{G}_{j,k+\frac{1}{2}}^{\text{FV}} - \frac{1}{24}(\Delta y)^2(\mathbf{G}_{yy})_{j,k+\frac{1}{2}} + \frac{7}{5760}(\Delta y)^4(\mathbf{G}_{yyyy})_{j,k+\frac{1}{2}}, \quad (4.6)$$

where the high-order correction terms are

$$\begin{aligned} (\mathbf{G}_{yy})_{j,k+\frac{1}{2}} &= \frac{-\mathcal{G}_{j,k-\frac{3}{2}}^{\text{FV}} + 16\mathcal{G}_{j,k-\frac{1}{2}}^{\text{FV}} - 30\mathcal{G}_{j,k+\frac{1}{2}}^{\text{FV}} + 16\mathcal{G}_{j,k+\frac{3}{2}}^{\text{FV}} - \mathcal{G}_{j,k+\frac{5}{2}}^{\text{FV}}}{12(\Delta y)^2}, \\ (\mathbf{G}_{yyyy})_{j,k+\frac{1}{2}} &= \frac{\mathcal{G}_{j,k-\frac{3}{2}}^{\text{FV}} - 4\mathcal{G}_{j,k-\frac{1}{2}}^{\text{FV}} + 6\mathcal{G}_{j,k+\frac{1}{2}}^{\text{FV}} - 4\mathcal{G}_{j,k+\frac{3}{2}}^{\text{FV}} + \mathcal{G}_{j,k+\frac{5}{2}}^{\text{FV}}}{(\Delta y)^4}. \end{aligned} \quad (4.7)$$

If  $(x_j, y_{k+\frac{1}{2}})$  is in Region RC, we set  $\mathcal{G}_{j,k+\frac{1}{2}} = \mathcal{G}_{j,k+\frac{1}{2}}^{\text{FV}}$ , coinciding with the 2-D second-order LDCU numerical flux from [11].

**Remark 4.1.** *We do not provide details on the 2-D CU and LDCU numerical fluxes for the sake brevity.*

Let us now address the computation of the required point values at cell interfaces. We obtain the point values  $\mathbf{U}_{j+\frac{1}{2},k}^{\pm}$  and  $\mathbf{U}_{j,k+\frac{1}{2}}^{\pm}$  as follows. If  $(x_{j+\frac{1}{2}}, y_k) \in$  Region S, we use the 1-D fourth-degree polynomials and compute fifth-order interpolants over the stencils  $\{(x_{j-2}, y_k), (x_{j-1}, y_k), (x_j, y_k), (x_{j+1}, y_k), (x_{j+2}, y_k)\}$  and  $\{(x_{j-1}, y_k), (x_j, y_k), (x_{j+1}, y_k), (x_{j+2}, y_k), (x_{j+3}, y_k)\}$  in the  $x$ -direction to obtain

$$\mathbf{U}_{j+\frac{1}{2},k}^- = \frac{3\mathbf{U}_{j-2,k} - 20\mathbf{U}_{j-1,k} + 90\mathbf{U}_{j,k} + 60\mathbf{U}_{j+1,k} - 5\mathbf{U}_{j+2,k}}{128}, \quad (4.8)$$

and

$$\mathbf{U}_{j+\frac{1}{2},k}^+ = \frac{-5\mathbf{U}_{j-1,k} + 60\mathbf{U}_{j,k} + 90\mathbf{U}_{j+1,k} - 20\mathbf{U}_{j+2,k} + 3\mathbf{U}_{j+3,k}}{128}, \quad (4.9)$$

respectively. Acting similarly in the  $y$ -direction, we obtain

$$\begin{aligned}\mathbf{U}_{j,k+\frac{1}{2}}^- &= \frac{3\mathbf{U}_{j,k-2} - 20\mathbf{U}_{j,k-1} + 90\mathbf{U}_{j,k} + 60\mathbf{U}_{j,k+1} - 5\mathbf{U}_{j,k+2}}{128}, \\ \mathbf{U}_{j,k+\frac{1}{2}}^+ &= \frac{-5\mathbf{U}_{j,k-1} + 60\mathbf{U}_{j,k} + 90\mathbf{U}_{j,k+1} - 20\mathbf{U}_{j,k+2} + 3\mathbf{U}_{j,k+3}}{128}.\end{aligned}\quad (4.10)$$

In “rough” regions, we proceed as in the 1-D case and perform the interpolation/reconstruction in local characteristic variables  $\boldsymbol{\Gamma}$ , which are obtained using the LCD in a dimension-by-dimension manner. In the  $x$ -direction, we first compute for all  $k$  averaged values  $\widehat{\mathbf{U}}_{j+\frac{1}{2},k}$  (in the numerical examples presented in §5, we have used the Roe averages) and define the local linearized Jacobians  $\widehat{\mathbf{A}}_{j+\frac{1}{2},k} := \frac{\partial \mathbf{F}}{\partial \mathbf{U}}(\widehat{\mathbf{U}}_{j+\frac{1}{2},k})$ , whose eigenvectors form the matrices  $R_{j+\frac{1}{2},k}$ . We then introduce the local characteristic variables in the neighborhood of  $(x_{j+\frac{1}{2}}, y_k)$ ,

$$\boldsymbol{\Gamma}_\ell := R_{j+\frac{1}{2},k}^{-1} \mathbf{U}_{\ell,k}, \quad \ell = j-2, \dots, j+3,$$

and obtain the values  $\boldsymbol{\Gamma}_{j+\frac{1}{2}}^\pm$  using the 1-D adaptive interpolation/reconstruction described in §3.2. After that, we obtain the corresponding point values of  $\mathbf{U}$  by

$$\mathbf{U}_{j+\frac{1}{2},k}^\pm = R_{j+\frac{1}{2},k} \boldsymbol{\Gamma}_{j+\frac{1}{2}}^\pm.$$

Finally, we proceed in the  $y$ -direction in a similar way to compute  $\widehat{\mathbf{U}}_{j,k+\frac{1}{2}}$  in “rough” regions.

### 4.3 Numerical Solver for the Primitive System

We employ the semi-discretization (4.3) with the 2-D fifth-order global numerical fluxes

$$\begin{aligned}\mathcal{K}_{j+\frac{1}{2},k} &= \mathcal{K}_{j+\frac{1}{2},k}^{\text{FV}} - \frac{1}{24}(\Delta x)^2 (\mathbf{K}_{xx})_{j+\frac{1}{2},k} + \frac{7}{5760}(\Delta x)^4 (\mathbf{K}_{xxxx})_{j+\frac{1}{2},k}, \\ \mathcal{L}_{j,k+\frac{1}{2}} &= \mathcal{L}_{j,k+\frac{1}{2}}^{\text{FV}} - \frac{1}{24}(\Delta y)^2 (\mathbf{L}_{yy})_{j,k+\frac{1}{2}} + \frac{7}{5760}(\Delta y)^4 (\mathbf{L}_{yyyy})_{j,k+\frac{1}{2}},\end{aligned}\quad (4.11)$$

where  $\mathcal{K}_{j+\frac{1}{2},k}^{\text{FV}}$  and  $\mathcal{L}_{j,k+\frac{1}{2}}^{\text{FV}}$  are dimension-by-dimension extensions of the 1-D numerical global fluxes introduced in §3.3 and the high-order correction terms are

$$\begin{aligned}(\mathbf{K}_{xx})_{j+\frac{1}{2},k} &= \frac{-\mathcal{K}_{j-\frac{3}{2},k}^{\text{FV}} + 16\mathcal{K}_{j-\frac{1}{2},k}^{\text{FV}} - 30\mathcal{K}_{j+\frac{1}{2},k}^{\text{FV}} + 16\mathcal{K}_{j+\frac{3}{2},k}^{\text{FV}} - \mathcal{K}_{j+\frac{5}{2},k}^{\text{FV}}}{12(\Delta x)^2}, \\ (\mathbf{K}_{xxxx})_{j+\frac{1}{2},k} &= \frac{\mathcal{K}_{j-\frac{3}{2},k}^{\text{FV}} - 4\mathcal{K}_{j-\frac{1}{2},k}^{\text{FV}} + 6\mathcal{K}_{j+\frac{1}{2},k}^{\text{FV}} - 4\mathcal{K}_{j+\frac{3}{2},k}^{\text{FV}} + \mathcal{K}_{j+\frac{5}{2},k}^{\text{FV}}}{(\Delta x)^4}, \\ (\mathbf{L}_{yy})_{j,k+\frac{1}{2}} &= \frac{-\mathcal{L}_{j,k-\frac{3}{2}}^{\text{FV}} + 16\mathcal{L}_{j,k-\frac{1}{2}}^{\text{FV}} - 30\mathcal{L}_{j,k+\frac{1}{2}}^{\text{FV}} + 16\mathcal{L}_{j,k+\frac{3}{2}}^{\text{FV}} - \mathcal{L}_{j,k+\frac{5}{2}}^{\text{FV}}}{12(\Delta y)^2}, \\ (\mathbf{L}_{xxxx})_{j,k+\frac{1}{2}} &= \frac{\mathcal{L}_{j,k-\frac{3}{2}}^{\text{FV}} - 4\mathcal{L}_{j,k-\frac{1}{2}}^{\text{FV}} + 6\mathcal{L}_{j,k+\frac{1}{2}}^{\text{FV}} - 4\mathcal{L}_{j,k+\frac{3}{2}}^{\text{FV}} + \mathcal{L}_{j,k+\frac{5}{2}}^{\text{FV}}}{(\Delta y)^4}.\end{aligned}\quad (4.12)$$

The finite-volume numerical global fluxes are given by

$$\begin{aligned} \mathcal{K}_{j+\frac{1}{2},k}^{\text{FV}} &= \frac{a_{j+\frac{1}{2},k}^+ \mathbf{K}_{j+\frac{1}{2},k}^- - a_{j+\frac{1}{2},k}^- \mathbf{K}_{j+\frac{1}{2},k}^+}{a_{j+\frac{1}{2},k}^+ - a_{j+\frac{1}{2},k}^-} \\ &\quad + \frac{a_{j+\frac{1}{2},k}^+ a_{j+\frac{1}{2},k}^-}{a_{j+\frac{1}{2},k}^+ - a_{j+\frac{1}{2},k}^-} \left( \mathbf{V}_{j+\frac{1}{2},k}^+ - \mathbf{V}_{j+\frac{1}{2},k}^- \right), \\ \mathcal{L}_{j,k+\frac{1}{2}}^{\text{FV}} &= \frac{a_{j,k+\frac{1}{2}}^+ \mathbf{L}_{j,k+\frac{1}{2}}^- - a_{j,k+\frac{1}{2}}^- \mathbf{L}_{j,k+\frac{1}{2}}^+}{a_{j,k+\frac{1}{2}}^+ - a_{j,k+\frac{1}{2}}^-} \\ &\quad + \frac{a_{j,k+\frac{1}{2}}^+ a_{j,k+\frac{1}{2}}^-}{a_{j,k+\frac{1}{2}}^+ - a_{j,k+\frac{1}{2}}^-} \left( \mathbf{V}_{j,k+\frac{1}{2}}^+ - \mathbf{V}_{j,k+\frac{1}{2}}^- \right), \end{aligned} \quad (4.13)$$

where  $\mathbf{V}_{j+\frac{1}{2},k}^\pm$  and  $\mathbf{V}_{j,k+\frac{1}{2}}^\pm$  are one-sided point values at  $(x_{j+\frac{1}{2}}, y_k)$  and  $(x_j, y_{k+\frac{1}{2}})$ , respectively. As in the 1-D case, these values are computed using the unlimited fifth-order (fourth-degree) interpolations performed in the  $x$ - and  $y$ -directions separately. This results in

$$\begin{aligned} \mathbf{V}_{j+\frac{1}{2},k}^- &= \frac{3\mathbf{V}_{j-2,k} - 20\mathbf{V}_{j-1,k} + 90\mathbf{V}_{j,k} + 60\mathbf{V}_{j+1,k} - 5\mathbf{V}_{j+2,k}}{128}, \\ \mathbf{V}_{j+\frac{1}{2},k}^+ &= \frac{-5\mathbf{V}_{j-1,k} + 60\mathbf{V}_{j,k} + 90\mathbf{V}_{j+1,k} - 20\mathbf{V}_{j+2,k} + 3\mathbf{V}_{j+3,k}}{128}, \\ \mathbf{V}_{j,k+\frac{1}{2}}^- &= \frac{3\mathbf{V}_{j,k-2} - 20\mathbf{V}_{j,k-1} + 90\mathbf{V}_{j,k} + 60\mathbf{V}_{j,k+1} - 5\mathbf{V}_{j,k+2}}{128}, \\ \mathbf{V}_{j,k+\frac{1}{2}}^+ &= \frac{-5\mathbf{V}_{j,k-1} + 60\mathbf{V}_{j,k} + 90\mathbf{V}_{j,k+1} - 20\mathbf{V}_{j,k+2} + 3\mathbf{V}_{j,k+3}}{128}. \end{aligned}$$

In (4.13),  $a_{j+\frac{1}{2},k}^\pm$  and  $a_{j,k+\frac{1}{2}}^\pm$  are the one-sided local speeds of propagation in the  $x$ - and  $y$ -directions, respectively. The speeds are estimated by

$$\begin{aligned} a_{j+\frac{1}{2},k}^+ &= \max \left\{ u_{j+\frac{1}{2},k}^- + c_{j+\frac{1}{2},k}^-, u_{j+\frac{1}{2},k}^+ + c_{j+\frac{1}{2},k}^+, \delta \right\}, \\ a_{j+\frac{1}{2},k}^- &= \min \left\{ u_{j+\frac{1}{2},k}^- - c_{j+\frac{1}{2},k}^-, u_{j+\frac{1}{2},k}^+ - c_{j+\frac{1}{2},k}^+, -\delta \right\}, \\ a_{j,k+\frac{1}{2}}^+ &= \max \left\{ v_{j,k+\frac{1}{2}}^- + c_{j,k+\frac{1}{2}}^-, v_{j,k+\frac{1}{2}}^+ + c_{j,k+\frac{1}{2}}^+, \delta \right\}, \\ a_{j,k+\frac{1}{2}}^- &= \min \left\{ v_{j,k+\frac{1}{2}}^- - c_{j,k+\frac{1}{2}}^-, v_{j,k+\frac{1}{2}}^+ - c_{j,k+\frac{1}{2}}^+, -\delta \right\}, \end{aligned} \quad (4.14)$$

where  $u_{j+\frac{1}{2},k}^\pm$  and  $c_{j+\frac{1}{2},k}^\pm$  are computed from  $\mathbf{V}_{j+\frac{1}{2},k}^\pm$ ,  $v_{j,k+\frac{1}{2}}^\pm$  and  $c_{j,k+\frac{1}{2}}^\pm$  are computed from  $\mathbf{V}_{j,k+\frac{1}{2}}^\pm$ , and  $\delta = 10^{-10}$ .

Finally, the global fluxes  $\mathbf{K}_{j+\frac{1}{2},k}^\pm$  and  $\mathbf{L}_{j,k+\frac{1}{2}}^\pm$  used in (4.13) are obtained by

$$\mathbf{K}_{j+\frac{1}{2},k}^\pm = \tilde{\mathbf{F}}(\mathbf{V}_{j+\frac{1}{2},k}^\pm) - \mathbf{R}_{j+\frac{1}{2},k}, \quad \mathbf{L}_{j,k+\frac{1}{2}}^\pm = \tilde{\mathbf{G}}(\mathbf{V}_{j,k+\frac{1}{2}}^\pm) - \mathbf{S}_{j,k+\frac{1}{2}}, \quad (4.15)$$

where the global part of the numerical flux is evaluated recursively by setting  $\hat{x} = x_{\frac{1}{2}}$  and  $\hat{y} = y_{\frac{1}{2}}$  so that  $\mathbf{R}_{\frac{1}{2},k} = \mathbf{S}_{j,\frac{1}{2}} = \mathbf{0}$ , and then computing

$$\begin{aligned}\mathbf{R}_{j+\frac{1}{2},k} &= \mathbf{R}_{j-\frac{1}{2},k} + \mathbf{B}_{j,k}, \quad j = 1, \dots, N, \\ \mathbf{S}_{j,k+\frac{1}{2}} &= \mathbf{S}_{j,k-\frac{1}{2}} + \mathbf{C}_{j,k}, \quad k = 1, \dots, M,\end{aligned}\tag{4.16}$$

where  $\mathbf{B}_j$  and  $\mathbf{C}_{j,k}$  are fifth-order approximations of the integrals of the nonconservative product terms:

$$\begin{aligned}\mathbf{B}_{j,k} &\approx \int_{x_{j-\frac{1}{2}}}^{x_{j+\frac{1}{2}}} B(\mathbf{V}) \mathbf{V}_x \, dx, \quad \mathbf{C}_{j,k} \approx \int_{y_{k-\frac{1}{2}}}^{y_{k+\frac{1}{2}}} C(\mathbf{V}) \mathbf{V}_y \, dy.\end{aligned}\tag{4.17}$$

We evaluate the first of these integrals using the fifth-order Newton-Cotes quadrature with the nodes  $(x_{j-\frac{1}{2}}, y_k)$ ,  $(x_{j-\frac{1}{4}}, y_k)$ ,  $(x_j, y_k)$ ,  $(x_{j+\frac{1}{4}}, y_k)$ ,  $(x_{j+\frac{1}{2}}, y_k)$ . When this quadrature is applied, one needs to interpolate the values  $\mathbf{V}_{j\pm\frac{1}{4},k}$  at the points  $(x_{j\pm\frac{1}{4}}, y_k)$ . This is done using the unlimited fifth-order (fourth-degree) polynomial interpolant over the stencil  $\{(x_{j-2}, y_k), (x_{j-1}, y_k), (x_j, y_k), (x_{j+1}, y_k), (x_{j+2}, y_k)\}$ , which gives

$$\begin{aligned}\mathbf{V}_{j-\frac{1}{4},k} &= \frac{-45\mathbf{V}_{j-2,k} + 420\mathbf{V}_{j-1,k} + 1890\mathbf{V}_{j,k} - 252\mathbf{V}_{j+1,k} + 35\mathbf{V}_{j+2,k}}{2048}, \\ \mathbf{V}_{j+\frac{1}{4},k} &= \frac{35\mathbf{V}_{j-2,k} - 252\mathbf{V}_{j-1,k} + 1890\mathbf{V}_{j,k} + 420\mathbf{V}_{j+1,k} - 45\mathbf{V}_{j+2,k}}{2048}.\end{aligned}\tag{4.18}$$

The second integral in (4.17) is evaluated using the same fifth-order Newton-Cotes quadrature, which would require the values  $\mathbf{V}_{j,k\pm\frac{1}{4}}$  at the points  $(x_j, y_{k\pm\frac{1}{4}})$ , which are computed similarly to (4.18):

$$\begin{aligned}\mathbf{V}_{j,k-\frac{1}{4}} &= \frac{-45\mathbf{V}_{j,k-2} + 420\mathbf{V}_{j,k-1} + 1890\mathbf{V}_{j,k} - 252\mathbf{V}_{j,k+1} + 35\mathbf{V}_{j,k+2}}{2048}, \\ \mathbf{V}_{j,k+\frac{1}{4}} &= \frac{35\mathbf{V}_{j,k-2} - 252\mathbf{V}_{j,k-1} + 1890\mathbf{V}_{j,k} + 420\mathbf{V}_{j,k+1} - 45\mathbf{V}_{j,k+2}}{2048}.\end{aligned}$$

## 5 Numerical Examples

In this section, we illustrate the performance of the proposed adaptive approach on benchmarks for the 1-D (§5.1) and 2-D (§5.2) Euler equations of gas dynamics.

In all of the numerical examples:

- The three-stages third-order strong stability-preserving (SSP) Runge-Kutta method [24,25] is employed to numerically integrate the ODE systems (3.4), (3.5), (4.2), and (4.3);
- The time step is selected with the CFL number 0.45;
- The first time evolution step is performed by the non-adaptive A-WENO schemes, which coincides with the A-WENO schemes used in the Regions RNC, but applied throughout the entire computational domain. These non-adaptive methods will be referred to as A-WENO schemes;
- $\gamma = 1.4$ , except for Example 6, in which  $\gamma = 5/3$ ;
- In addition, the symmetry-enforcing algorithm from [51, Appendix B] is implemented in 2-D examples.

In order to demonstrate the advantages of the proposed adaptive methods, we compare the obtained results with those computed by the non-adaptive A-WENO schemes.

**Remark 5.1.** While conducting the numerical experiments, we have observed that the distribution of smooth and “rough” areas over the computational domain varies only slightly over a short time interval. Therefore, computational cost can be reduced by avoiding shock detection at every time step. In fact, in all of the numerical experiments reported below, the shock detection is performed only once every three time steps and the Regions  $S$ ,  $RC$ , and  $RNC$  are kept unchanged until the next shock detection is carried out.

**Remark 5.2.** In the case the solution is smooth, our adaptive scheme reduces to the fifth-order A-WENO scheme with the unlimited reconstruction. We have verified that the experimental order of convergence (EOC) is the expected fifth one on several 1-D and 2-D accuracy tests, not reported here for the sake of brevity. We stress that when the EOC was checked, the time step was adjusted to be proportional to  $(\Delta x)^{\frac{5}{3}}$  in order to guarantee a matching between the temporal and spatial accuracy.

## 5.1 One-Dimensional Examples

The 1-D tests discussed in this section include two shock-turbulence interaction problems characterized by several smooth structures and a blast wave problem featuring strong discontinuities.

**Example 1 (Shock-Density Wave Interaction Problem)** In this example, we consider the shock-density wave interaction problem originally proposed in [46]. The initial conditions,

$$(\rho(x, 0), u(x, 0), p(x, 0)) = \begin{cases} \left(\frac{27}{7}, \frac{4\sqrt{35}}{9}, \frac{31}{3}\right), & x < -4, \\ (1 + 0.2 \sin(5x), 0, 1), & x > -4, \end{cases}$$

are prescribed in the computational domain  $[-5, 15]$  subject to the free boundary conditions. In this case, a Mach 3 shock interacts with small-amplitude density fluctuations ahead of it, generating a sequence of intricate waves behind the shock.

We compute the numerical solutions by the adaptive (with the adaption coefficients  $\kappa_{\rho u} = 10^{-3}$  and  $\kappa_p = 10^{-5}$ ) and A-WENO schemes until the final time  $t = 5$  on a uniform mesh with  $\Delta x = 1/30$ . The numerical results are shown in Figure 5.1 along with the reference solution obtained by the A-WENO scheme on a much finer uniform mesh with  $\Delta x = 1/400$ . As can be observed, the adaptive scheme produces results that are only slightly better than those obtained by the A-WENO scheme. However, the CPU time consumed by the adaptive scheme is substantially smaller than that consumed by the A-WENO scheme, which performs Ai-WENO-Z interpolations throughout the entire computational domain. Therefore, to assess the efficiency of the proposed adaptive strategy, we rerun the adaptive scheme on a finer mesh with  $\Delta x = 2/87$ , while keeping the CPU time identical to that of the A-WENO scheme on the mesh with  $\Delta x = 1/30$ . The obtained results are shown in Figure 5.2, where one can see that for the same computational cost, the adaptive scheme clearly outperforms the A-WENO scheme.

**Example 2 (Shock-Entropy Wave Interaction Problem)** In this example, we consider the shock-entropy wave interaction problem taken from [47]. The initial conditions,

$$(\rho(x, 0), u(x, 0), p(x, 0)) = \begin{cases} (1.51695, 0.523346, 1.805), & x < -4.5, \\ (1 + 0.1 \sin(20x), 0, 1), & x > -4.5, \end{cases}$$

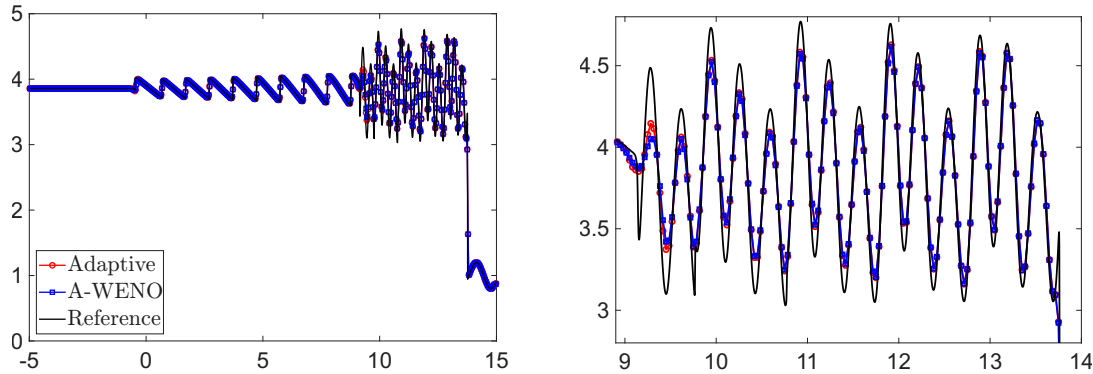


Figure 5.1: Example 1: Density  $\rho$  computed by the adaptive and A-WENO scheme with  $\Delta x = 1/30$  (left) and zoom at  $x \in [8.9, 14]$  (right).

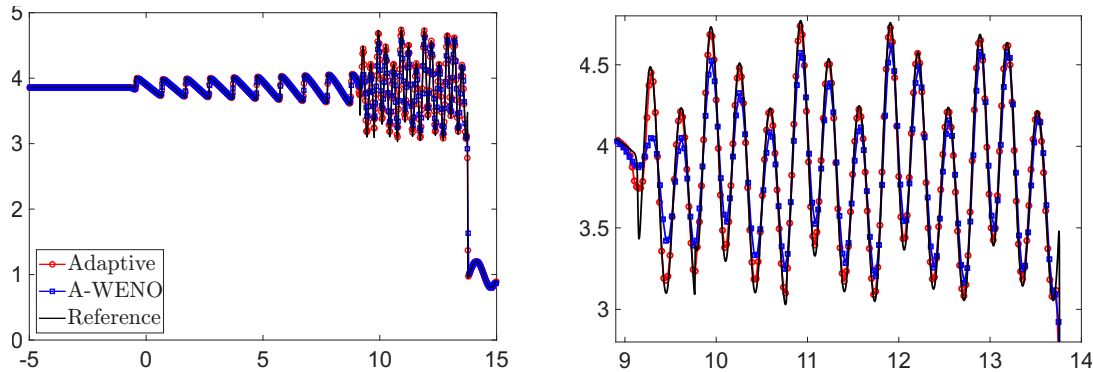


Figure 5.2: Example 1: Density  $\rho$  computed by the adaptive and A-WENO scheme with  $\Delta x = 2/87$  and  $\Delta x = 1/30$ , respectively (left) and zoom at  $x \in [8.9, 14]$  (right).

are prescribed in the computational domain  $[-5, 5]$  subject to the free boundary conditions. This test illustrates the interaction between a Mach 1.1 forward-facing shock and small-scale density fluctuations. As the shock propagates downstream, the perturbations are convected and amplified ahead of it, leading to the formation of high-frequency entropy waves.

We compute the numerical solutions by the adaptive (with the adaption coefficients  $\kappa_{\rho u} = 5 \cdot 10^{-3}$  and  $\kappa_p = 10^{-3}$ ) and A-WENO schemes until the final time  $t = 5$ . As in the previous example, we have observed that the adaptive and A-WENO schemes produce very similar computed solutions when implemented on the same meshes. However, in order to perform a fair comparison between the investigated methods, we conduct the simulations on meshes, which would require the same CPU times for both methods. The obtained numerical results are reported in Figure 5.3 along with a reference solution computed using the A-WENO scheme on a much finer uniform mesh with  $\Delta x = 1/800$ . In particular, the adaptive scheme is applied on a uniform mesh with  $\Delta x = 2/105$ , whereas the A-WENO scheme is computed on a coarser mesh with  $\Delta x = 1/40$ . As illustrated in the right panel, which zooms in on the interval  $[-0.9, 1.6]$  containing high-frequency wave structures, the adaptive scheme achieves noticeably higher resolution compared to the A-WENO one.

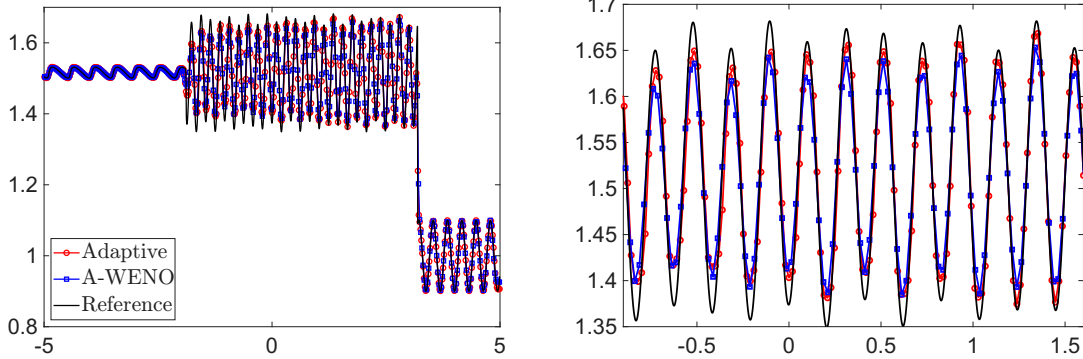


Figure 5.3: Example 2: Density  $\rho$  computed by the adaptive and A-WENO scheme with  $\Delta x = 2/105$  and  $\Delta x = 1/40$ , respectively (left) and zoom at  $x \in [-0.9, 1.6]$  (right).

**Example 3 (Blast Wave Problem)** In the final 1-D example, we consider the blast wave problem proposed in [54]. The initial conditions,

$$(\rho(x, 0), u(x, 0), p(x, 0)) = \begin{cases} (1, 0, 1000), & x < 0.1, \\ (1, 0, 0.01), & 0.1 < x < 0.9, \\ (1, 0, 100), & x > 0.9, \end{cases}$$

are imposed in the computational domain  $[0, 1]$  subject to the solid wall boundary conditions.

We compute the numerical solutions by the adaptive (with the adaption coefficients  $\kappa_{\rho u} = 10^{-4}$  and  $\kappa_p = 5 \cdot 10^{-2}$ ) and A-WENO schemes until the final time  $t = 0.038$  on a uniform mesh with  $\Delta x = 1/400$ . The obtained results are shown in Figure 5.4 along with the reference solution computed by the A-WENO scheme on a much finer mesh with  $\Delta x = 1/8000$ . As one can see, the adaptive scheme resolves the contact wave near  $x \in [0.59, 0.60]$  significantly sharper than the A-WENO scheme. This improvement is attributed to SI, which correctly identifies Region RC. Consequently, the overcompressive SBM reconstruction together with the LDCU numerical fluxes is activated near the contact waves, leading to their enhanced resolution.

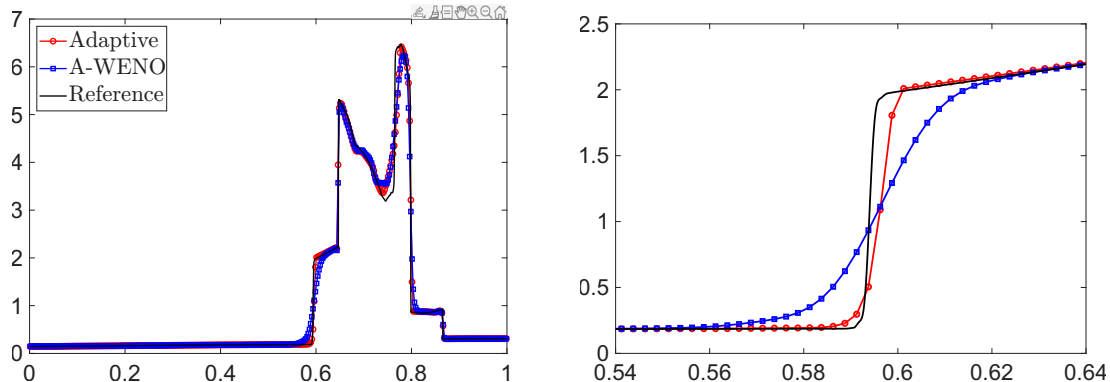


Figure 5.4: Example 3: Density  $\rho$  (left) and zoom at  $x \in [0.56, 0.62]$  (right).

## 5.2 Two-Dimensional Examples

The 2-D numerical examples include two 2-D Riemann problems with strong discontinuities as well as the implosion problem and the Rayleigh-Taylor (RT) instability problem, both featuring strong shocks and complex wave interactions.

In all of the 2-D examples presented below, we report plots of the different regions of the computational domain identified by the SIs at the final time. Specifically, the areas classified as Regions S, RC, and RNC based on the SIs in the  $x$ - and  $y$ -directions are displayed using three different colors: blue, green, and red, respectively.

**Example 4 (Riemann Problems)** In this example, we consider two Riemann problems from [35] with the following two sets of initial data:

$$\text{Configuration 3: } (\rho, u, v, p) |_{(x,y,0)} = \begin{cases} (1.5, 0, 0, 1.5), & x > 1, y > 1, \\ (0.5323, 1.206, 0, 0.3), & x < 1, y > 1, \\ (0.138, 1.206, 1.206, 0.029), & x < 1, y < 1, \\ (0.5323, 0, 1.206, 0.3), & x > 1, y < 1, \end{cases}$$

prescribed in the computational domain  $[0, 1.2] \times [0, 1.2]$ ;

$$\text{Configuration 12: } (\rho, u, v, p) |_{(x,y,0)} = \begin{cases} (0.5313, 0, 0, 0.4), & x > 0.5, y > 0.5, \\ (1, 0.7276, 0, 1), & x < 0.5, y > 0.5, \\ (0.8, 0, 0, 1), & x < 0.5, y < 0.5, \\ (1, 0, 0.7276, 1), & x > 0.5, y < 0.5, \end{cases}$$

prescribed in the computational domain  $[0, 0.6] \times [0, 0.6]$ . For both configurations, the free boundary conditions are imposed.

We begin with Configuration 3 and compute the numerical solutions by the adaptive (with the adaption coefficients  $\kappa_{\rho u} = \kappa_{\rho v} = 10^{-2}$  and  $\kappa_p = 5 \cdot 10^{-2}$ ) and A-WENO schemes until the final time  $t = 1$  on a uniform mesh with  $\Delta x = \Delta y = 3/1000$ . The numerical results are presented in Figure 5.5, where one can see that both methods accurately capture the complex interaction of four shocks and the resulting mushroom-shaped vortical structures. Notably, the proposed adaptive scheme resolves the fine-scale Kelvin-Helmholtz instabilities with lower numerical dissipation. To demonstrate the robustness of the proposed adaptive scheme in terms of the independence on the choice of the adaption coefficients on the mesh size, we refine the mesh to  $\Delta x = \Delta y = 3/2000$  and conduct the same simulations. The obtained results are displayed in Figure 5.6. One can observe that the adaptive scheme still clearly outperforms the A-WENO scheme in resolving complex wave structures. On both meshes, Regions S, RC, and RNC are adequately indicated, as can be seen in the bottom rows in Figures 5.5 and 5.6.

Next, we compute the numerical solutions for Configuration 12 using both the adaptive (with the adaption coefficients  $\kappa_{\rho u} = \kappa_{\rho v} = 0.9$  and  $\kappa_p = 1$ ) and A-WENO schemes until the final time  $t = 0.5$ . The numerical results, obtained on two uniform meshes with  $\Delta x = \Delta y = 3/2000$  and  $3/4000$ , are presented in Figures 5.7 and 5.8, respectively. It is evident that the adaptive scheme yields sharper resolution and finer-scale wave structures than its A-WENO counterpart, and that Regions S, RC, and RNC are adequately indicated.

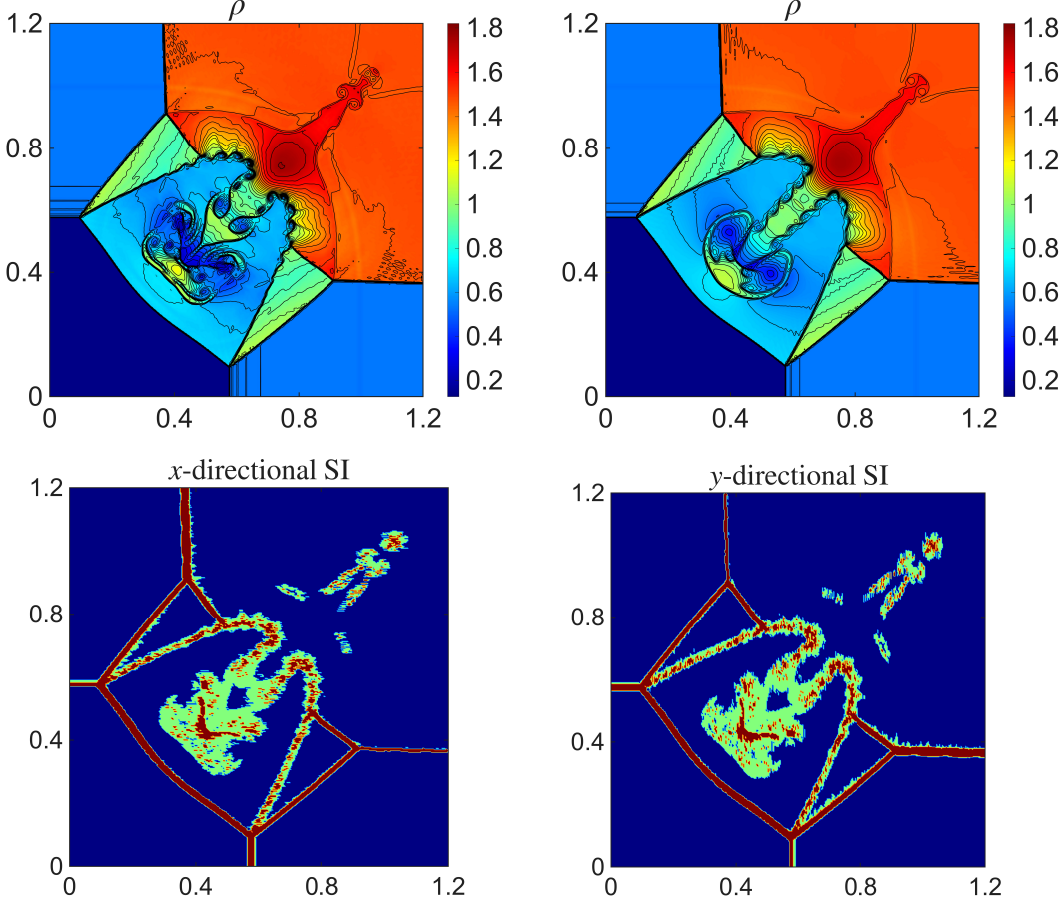


Figure 5.5: Example 4 (Configuration 3): Density  $\rho$  computed by the adaptive (top left) and A-WENO (top right) schemes on a uniform mesh with  $\Delta x = \Delta y = 3/1000$ , along with SIs in the  $x$ -direction (bottom left) and  $y$ -direction (bottom right).

**Example 5 (Implosion problem)** In this section, we consider the implosion problem taken from [38]. The initial conditions,

$$(\rho(x, y, 0), u(x, y, 0), v(x, y, 0), p(x, y, 0)) = \begin{cases} (0.125, 0, 0, 0.14), & x + y < 0.15, \\ (1, 0, 0, 1), & \text{otherwise,} \end{cases}$$

are prescribed in the computational domain  $[0, 0.3] \times [0, 0.3]$  subject to the solid wall boundary conditions. As time evolves, the surrounding high-density fluid converges toward the origin, compressing the low-density core and giving rise to a sequence of complex wave interactions, including multiple reflections and the eventual formation of a prominent jet-like structure that propagates along the symmetry line  $y = x$ .

We compute the numerical solutions by the adaptive (with the adaption coefficients  $\kappa_{\rho u} = \kappa_{\rho v} = 5 \cdot 10^{-2}$  and  $\kappa_p = 2 \cdot 10^{-2}$ ) and A-WENO schemes until the final time  $t = 2.5$  on two uniform meshes with  $\Delta x = \Delta y = 3/2500$  and  $3/4000$ , and plot the obtained solutions in Figures 5.9 and 5.10, respectively. As one can observe, the jet in the adaptive solution reaches further along the diagonal with sharper interfaces compared to the result obtained by the A-WENO scheme, indicating that the adaptive strategy effectively reduces numerical dissipation. These results demonstrate that the proposed adaptive scheme achieves superior resolution in capturing fine-scale flow structures and high-gradient phenomena without

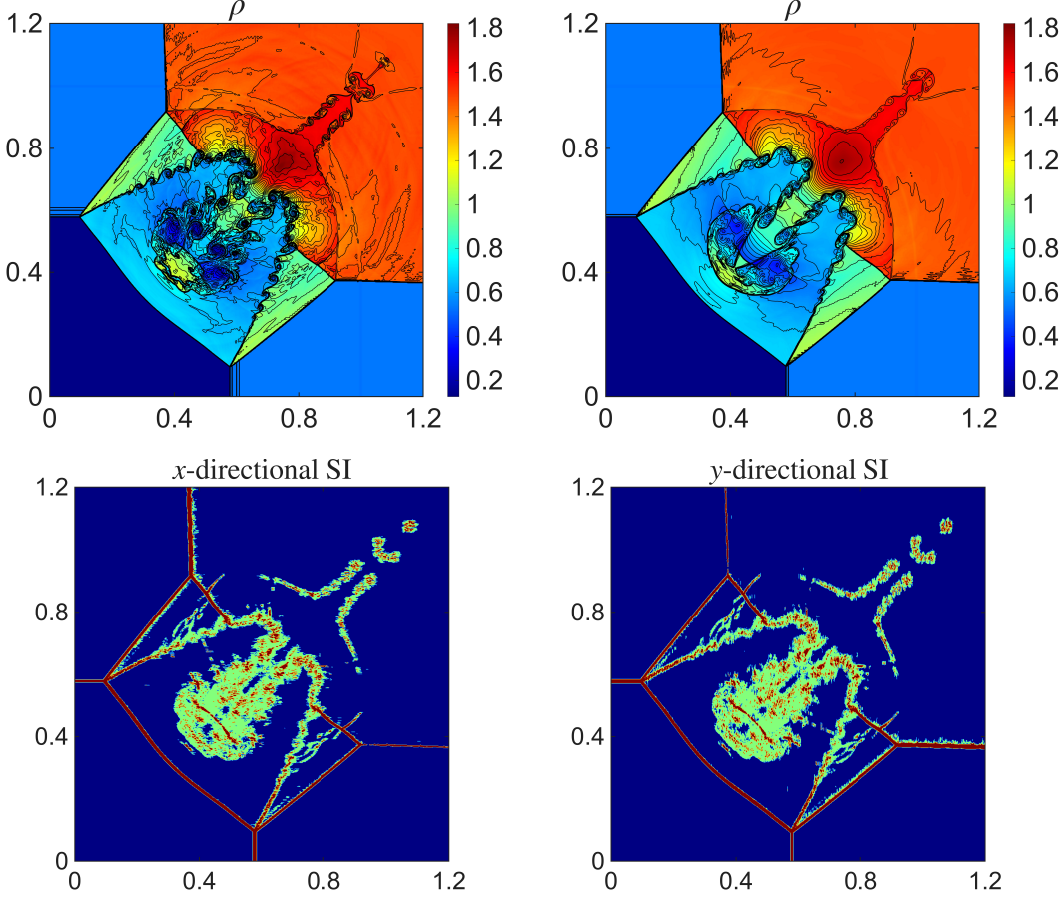


Figure 5.6: Example 4 (Configuration 3): Same as in Figure 5.5 but for the mesh with  $\Delta x = \Delta y = 3/2000$ .

introducing spurious oscillations. In addition, one can see that Regions S, RC, and RNC are adequately indicated.

**Example 6 (Rayleigh-Taylor Instability)** In the final example, we consider the RT instability, which arises at the interface between heavier and lighter fluids under the action of gravity. To incorporate gravitational effects, appropriate source terms are added to the vertical momentum and total energy equations. As a result, the governing equations become the 2-D compressible Euler equations with gravity, written as

$$\mathbf{U}_t + \mathbf{F}(\mathbf{U})_x + \mathbf{G}(\mathbf{U})_y = \mathbf{S},$$

where  $\mathbf{U}$ ,  $\mathbf{F}$  and  $\mathbf{G}$  are given by (1.3) and  $\mathbf{S} = (0, 0, \rho, \rho v)^\top$ .

The initial data,

$$(\rho, u, v, p) |_{(x,y,0)} = \begin{cases} (2, 0, -0.025c \cos(8\pi x), 2y + 1), & y < 0.5, \\ (1, 0, -0.025c \cos(8\pi x), y + 1.5), & y > 0.5, \end{cases}$$

with  $c$  being the speed of sound, are prescribed in the computational domain  $[0, 0.25] \times [0, 1]$  subject to the solid wall boundary conditions at the left and right boundaries and the following Dirichlet boundary

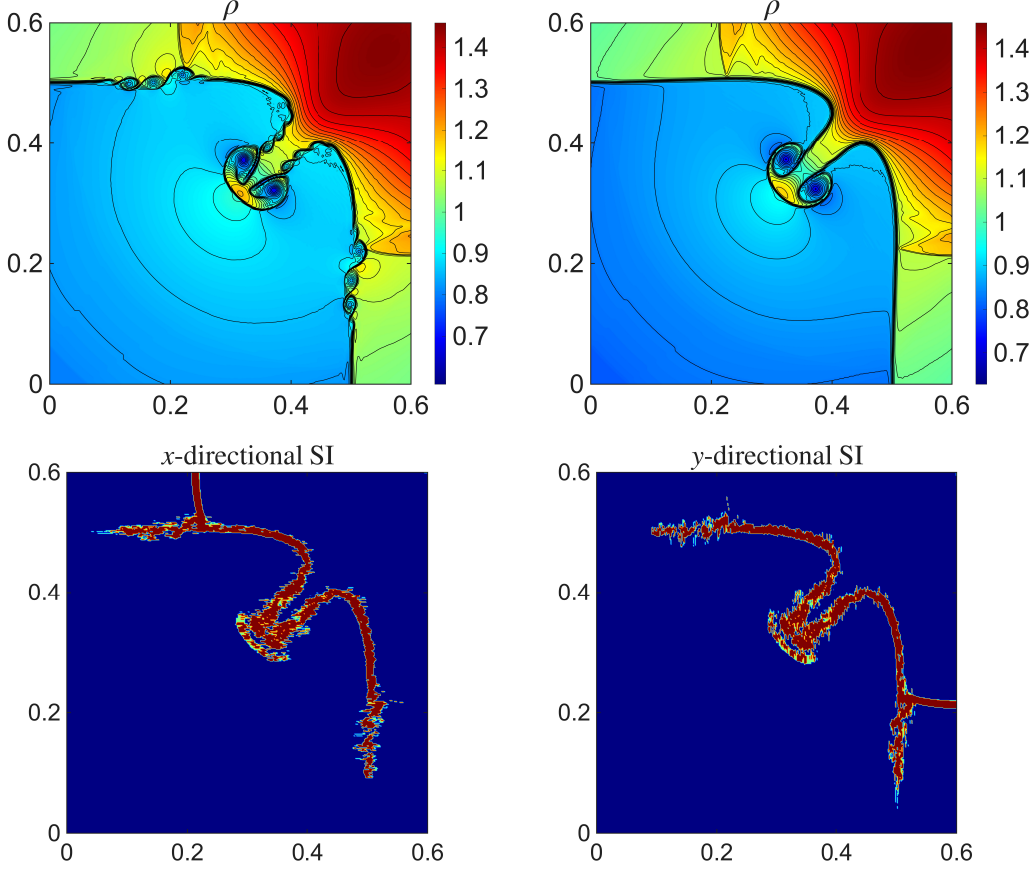


Figure 5.7: Example 4 (Configuration 12): Density  $\rho$  computed by the adaptive (top left) and A-WENO (top right) schemes on a uniform mesh with  $\Delta x = \Delta y = 3/2000$ , along with SIs in the  $x$ -direction (bottom left) and  $y$ -direction (bottom right).

conditions at the top and bottom boundaries:

$$(\rho, u, v, p) |_{(x, 1, t)} = (1, 0, 0, 2.5), \quad (\rho, u, v, p) |_{(x, 0, t)} = (2, 0, 0, 1).$$

We compute the numerical solutions by the adaptive (with the adaption coefficients  $\kappa_{\rho u} = \kappa_{\rho v} = 1.2$  and  $\kappa_p = 1$ ) and A-WENO schemes until the final time  $t = 2.95$  on a uniform mesh with  $\Delta x = \Delta y = 1/600$ . The density computed at times  $t = 1.95$  and  $2.95$  is shown in Figure 5.11, in which one can observe that the adaptive scheme resolves finer features, including Kelvin–Helmholtz roll-ups in the falling fluid, which are significantly smeared or entirely absent in the A-WENO results. Moreover, the SIs shown in the right columns demonstrate that the adaptive scheme accurately detects regions with strong gradients, thereby enabling sharper resolution of complex interfaces and vortical structures.

## 6 Conclusions

In this paper, we have developed new adaptive high-order numerical methods for hyperbolic systems of conservation laws within a dual formulation (DF) framework. The key idea is to simultaneously evolve, at each time step, solutions of both the conservative and nonconservative formulations of the same governing

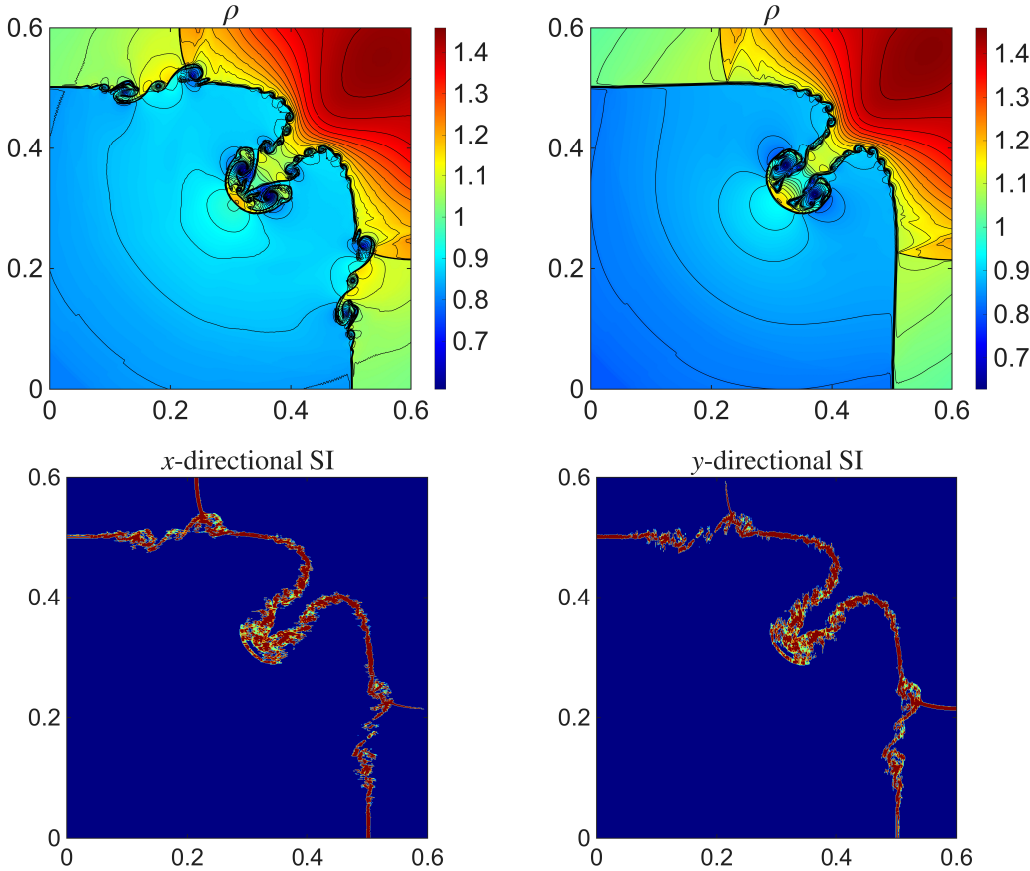


Figure 5.8: Example 4 (Configuration 12): Same as in Figure 5.7 but for the mesh with  $\Delta x = \Delta y = 3/4000$ .

system and exploiting the discrepancy between the resulting numerical solutions to develop reliable adaptive criteria. In particular, the smoothness indicator (SI) introduced in this work relies on the difference between the numerical solutions computed by the conservative and nonconservative schemes. While the two solutions remain close up to truncation errors in smooth regions, their difference becomes  $\mathcal{O}(1)$  in non-smooth regions. For the Euler equations of gas dynamics, the use of momentum- and pressure-based SIs makes it possible to distinguish between the neighborhoods of contact discontinuities and other “rough” parts of the computed solutions. This information is then used to adaptively select appropriate numerical discretizations across the computational domain. In the vicinities of contact discontinuities, we employ the low-dissipation central-upwind numerical flux and a second-order piecewise linear reconstruction with the slopes computed using an overcompressive SBM limiter. Elsewhere, we use an alternative weighted essentially non-oscillatory (A-WENO) framework with the central-upwind finite-volume numerical fluxes and either unlimited (in smooth regions) or Ai-WENO-Z (in the nonsmooth regions away from contact discontinuities) fifth-order interpolation.

Extensive one- and two-dimensional numerical experiments confirm that the proposed adaptive approach achieves a favorable balance between accuracy and efficiency. Compared with classical non-adaptive high-order schemes, the new method provides an improved resolution of complex solution structures at a significantly reduced computational cost. Overall, the results demonstrate that the DF-based adaptive paradigm offers a flexible and effective framework for the numerical simulation of problems involving intricate interactions between smooth and nonsmooth solution features. The reliance on prim-

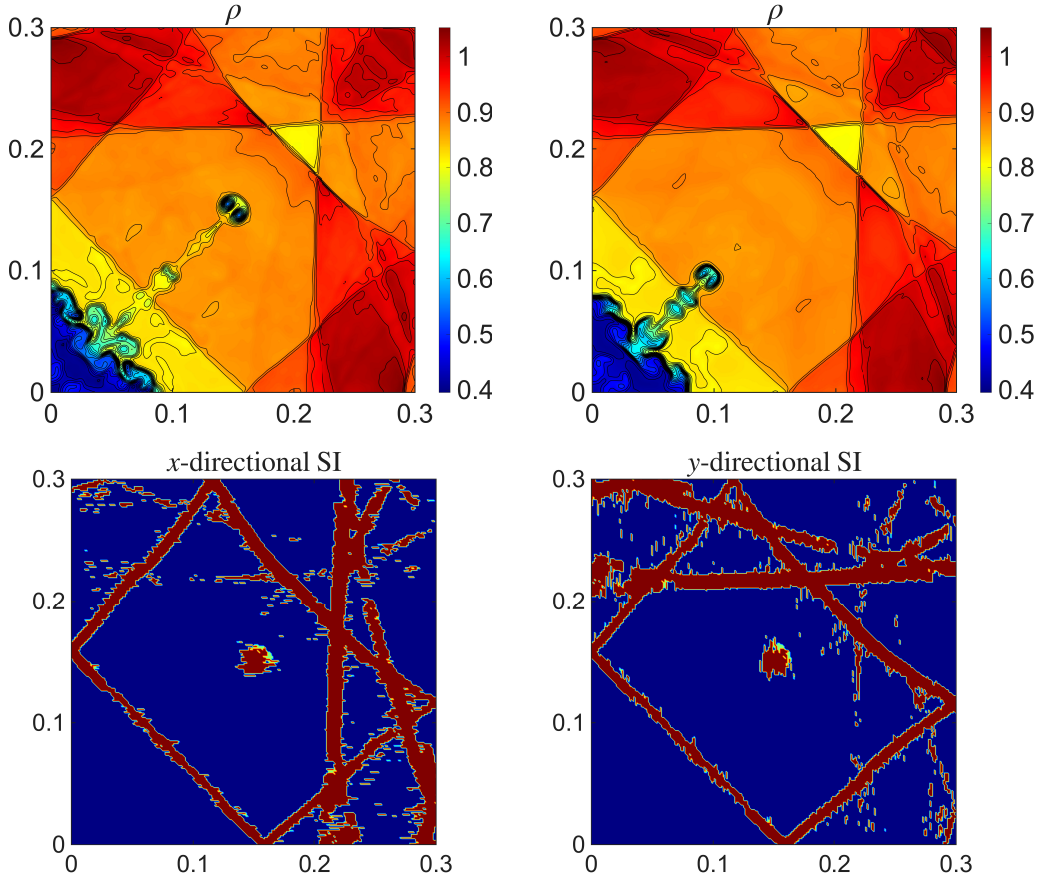


Figure 5.9: Example 5: Density  $\rho$  computed by the adaptive (top left) and A-WENO schemes (top right), along with SIs in the  $x$ -direction (bottom left) and the  $y$ -direction (bottom right). All with  $\Delta x = 3/2500$ .

itive formulations of the governing equations turns out to be particularly useful in many contexts. Our DF-approach offers a flexible way to exploit it, and further applications in various directions, including compressible multifluid flows and development of asymptotic-preserving schemes for a variety of hyperbolic systems of conservation laws, are currently under investigation by the authors.

## References

- [1] R. ABGRALL, *A combination of residual distribution and the active flux formulations or a new class of schemes that can combine several writings of the same hyperbolic problem: application to the 1D Euler equations*, Commun. Appl. Math. Comput., 5 (2023), pp. 370–402.
- [2] R. ABGRALL, A. CHERTOCK, A. KURGANOV, AND L. MICALIZZI, *Dual formulation finite-volume methods on overlapping meshes for hyperbolic conservation laws*, Comput. & Fluids, 307 (2026). Paper No. 106952.
- [3] R. ABGRALL, M. JIAO, Y. LIU, AND K. WU, *Bound-preserving point-average-moment polynomial-interpreted (PAMPA) scheme: one-dimensional case*, Commun. Comput. Phys., 39 (2026), pp. 29–58.

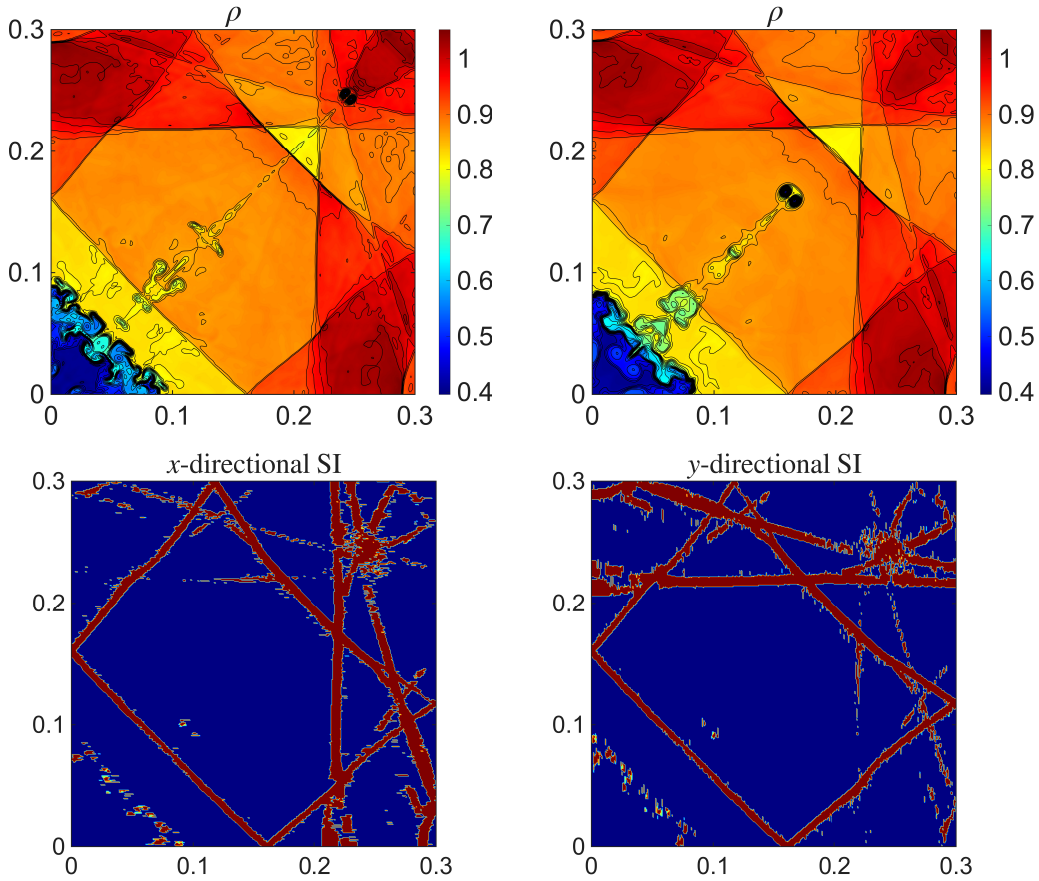


Figure 5.10: Example 5: Same as in Figure 5.9 but with  $\Delta x = 3/4000$ .

- [4] R. ABGRALL AND S. KARNI, *A comment on the computation of non-conservative products*, J. Comput. Phys., 229 (2010), pp. 2759–2763.
- [5] R. ABGRALL AND Y. LIU, *A new approach for designing well-balanced schemes for the shallow water equations: a combination of conservative and primitive formulations*, SIAM J. Sci. Comput., 46 (2024), pp. A3375–A3400.
- [6] F. ARÀNDIGA, A. BAEZA, AND R. DONAT, *Vector cell-average multiresolution based on Hermite interpolation*, Adv. Comput. Math., 28 (2008), pp. 1–22.
- [7] A. CHERTOCK, S. CHU, AND A. KURGANOV, *Adaptive high-order A-WENO schemes based on a new local smoothness indicator*, East Asian J. Appl. Math., 13 (2023), pp. 576–609.
- [8] A. CHERTOCK, A. KURGANOV, AND L. MICALIZZI, *New smoothness indicator within an active flux framework*, in Proceedings of the XIX International Conference on Hyperbolic Problems: Theory, Numerics and Applications, 2025. Accepted; arXiv:2505.00809.
- [9] S. CHU, A. KURGANOV, AND I. MENSHOV, *New adaptive low-dissipation central-upwind schemes*, Appl. Numer. Math., 209 (2025), pp. 155–170.
- [10] S. CHU, A. KURGANOV, AND M. NA, *Fifth-order A-WENO schemes based on the path-conservative central-upwind method*, J. Comput. Phys., 469 (2022). Paper No. 111508.

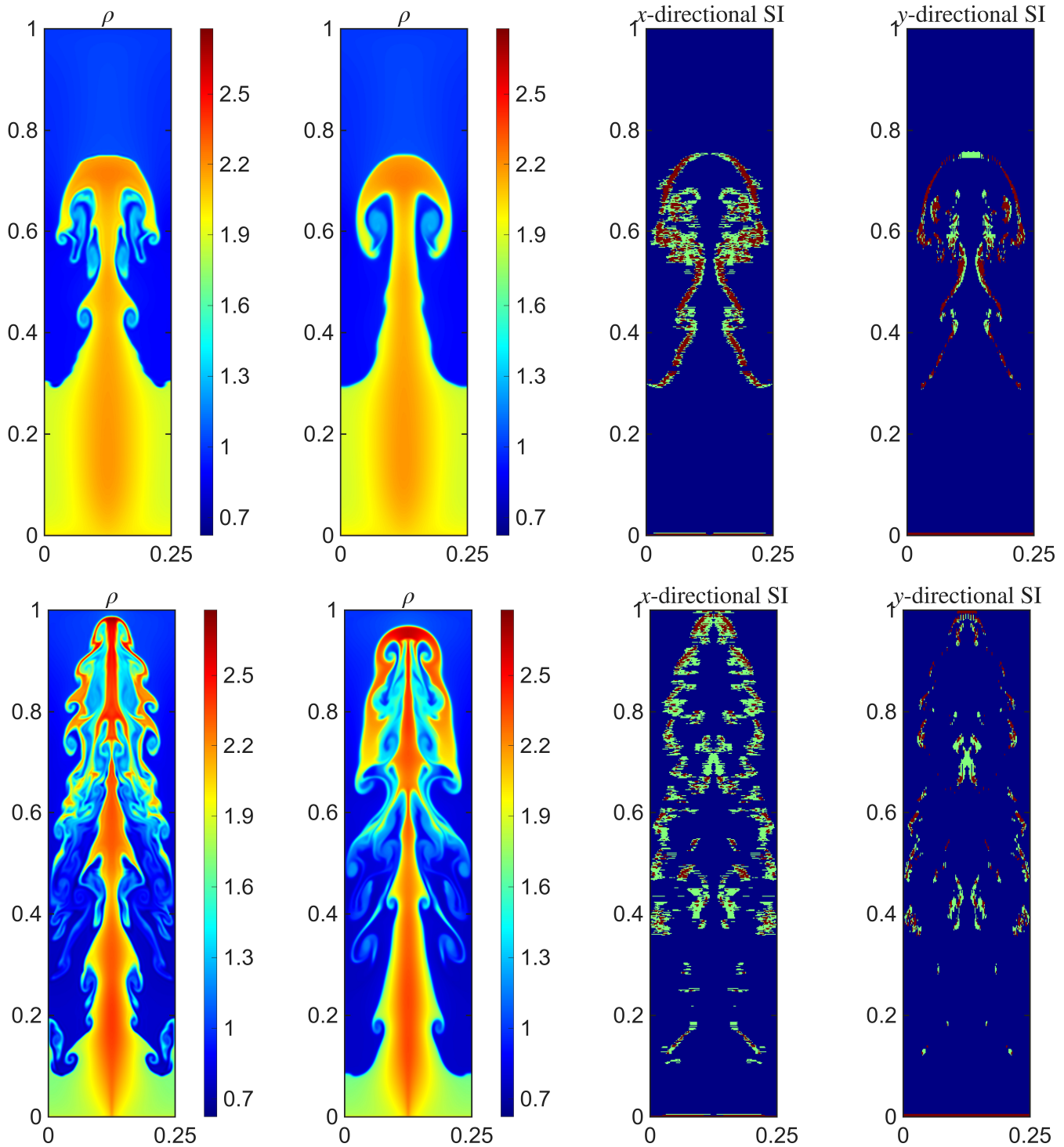


Figure 5.11: Example 6: Density  $\rho$  computed by the adaptive (left column) and A-WENO (second column) schemes, along with SIs in the  $x$ -direction (third column) and the  $y$ -direction (right column) at times  $t = 1.95$  (upper row) and at  $t = 2.95$  (bottom row).

[11] S. CHU, A. KURGANOV, AND R. XIN, *New low-dissipation central-upwind schemes. Part II*, J. Sci. Comput., 103 (2025). Paper No. 33.

- [12] ——, *New more efficient A-WENO schemes*, J. Sci. Comput., 104 (2025). Paper No. 53.
- [13] ——, *A well-balanced fifth-order A-WENO scheme based on flux globalization*, Beijing J. of Pure and Appl. Math., 2 (2025), pp. 87–113.
- [14] B. COSTA AND W. S. DON, *Multi-domain hybrid spectral-WENO methods for hyperbolic conservation laws*, J. Comput. Phys., 224 (2007), pp. 970–991.
- [15] J. DEWAR, A. KURGANOV, AND M. LEOPOLD, *Pressure-based adaption indicator for compressible Euler equations*, Numer. Methods Partial Differential Equations, 31 (2015), pp. 1844–1874.
- [16] W. S. DON, B.-S. WANG, AND Z. GAO, *Fast iterative adaptive multi-quadric radial basis function method for edges detection of piecewise functions—I: uniform mesh*, J. Sci. Comput., 75 (2018), pp. 1016–1039.
- [17] G. FU AND C.-W. SHU, *A new troubled-cell indicator for discontinuous Galerkin methods for hyperbolic conservation laws*, J. Comput. Phys., 347 (2017), pp. 305–327.
- [18] Q. FU, Y. GU, A. KURGANOV, AND B.-S. WANG, *Bound- and positivity-preserving path-conservative central-upwind AWENO scheme for the five-equation model of compressible two-component flows*, J. Sci. Comput., 104 (2025). Paper No. 94.
- [19] E. GABURRO, W. BOSCHERI, S. CHIOCCHETTI, AND M. RICCHIUTO, *Discontinuous Galerkin schemes for hyperbolic systems in non-conservative variables: quasi-conservative formulation with subcell finite volume corrections*, Comput. Methods Appl. Mech. Engrg., 431 (2024). Paper No. 117311.
- [20] Z. GAO, L.-L. FANG, B.-S. WANG, Y. WANG, AND W. S. DON, *Seventh and ninth orders alternative WENO finite difference schemes for hyperbolic conservation laws*, Comput. & Fluids, 202 (2020). Paper No. 104519.
- [21] A. GELB AND E. TADMOR, *Spectral reconstruction of piecewise smooth functions from their discrete data*, M2AN Math. Model. Numer. Anal., 36 (2002), pp. 155–175.
- [22] ——, *Adaptive edge detectors for piecewise smooth data based on the minmod limiter*, J. Sci. Comput., 28 (2006), pp. 279–306.
- [23] E. GODLEWSKI AND P.-A. RAVIART, *Numerical approximation of hyperbolic systems of conservation laws*, vol. 118 of Applied Mathematical Sciences, Springer-Verlag, New York, 2021. Second edition.
- [24] S. GOTTLIEB, D. KETCHESON, AND C.-W. SHU, *Strong stability preserving Runge-Kutta and multistep time discretizations*, World Scientific Publishing Co. Pte. Ltd., Hackensack, NJ, 2011.
- [25] S. GOTTLIEB, C.-W. SHU, AND E. TADMOR, *Strong stability-preserving high-order time discretization methods*, SIAM Rev., 43 (2001), pp. 89–112.
- [26] J.-L. GUERMOND, R. PASQUETTI, AND B. POPOV, *Entropy viscosity method for nonlinear conservation laws*, J. Comput. Phys., 230 (2011), pp. 4248–4267.

- [27] J. S. HESTHAVEN, *Numerical Methods for Conservation Laws: From Analysis to Algorithms*, vol. 18 of Computational Science & Engineering, Society for Industrial and Applied Mathematics (SIAM), Philadelphia, PA, 2018. From analysis to algorithms.
- [28] T. Y. HOU AND P. G. LEFLOCH, *Why nonconservative schemes converge to wrong solutions: error analysis*, Math. Comp., 62 (1994), pp. 497–530.
- [29] G.-S. JIANG AND C.-W. SHU, *Efficient implementation of weighted ENO schemes*, J. Comput. Phys., 126 (1996), pp. 202–228.
- [30] Y. JIANG, C.-W. SHU, AND M. P. ZHANG, *An alternative formulation of finite difference weighted ENO schemes with Lax-Wendroff time discretization for conservation laws*, SIAM J. Sci. Comput., 35 (2013), pp. A1137–A1160.
- [31] S. KARNI AND A. KURGANOV, *Local error analysis for approximate solutions of hyperbolic conservation laws*, Adv. Comput. Math., 22 (2005), pp. 79–99.
- [32] S. KARNI, A. KURGANOV, AND G. PETROVA, *A smoothness indicator for adaptive algorithms for hyperbolic systems*, J. Comput. Phys., 178 (2002), pp. 323–341.
- [33] A. KURGANOV AND C.-T. LIN, *On the reduction of numerical dissipation in central-upwind schemes*, Commun. Comput. Phys., 2 (2007), pp. 141–163.
- [34] A. KURGANOV AND Y. LIU, *New adaptive artificial viscosity method for hyperbolic systems of conservation laws*, J. Comput. Phys., 231 (2012), pp. 8114–8132.
- [35] A. KURGANOV AND E. TADMOR, *Solution of two-dimensional Riemann problems for gas dynamics without Riemann problem solvers*, Numer. Methods Partial Differential Equations, 18 (2002), pp. 584–608.
- [36] R. J. LEVEQUE, *Finite volume methods for hyperbolic problems*, Cambridge Texts in Applied Mathematics, Cambridge University Press, Cambridge, 2002.
- [37] K.-A. LIE AND S. NOELLE, *On the artificial compression method for second-order nonoscillatory central difference schemes for systems of conservation laws*, SIAM J. Sci. Comput., 24 (2003), pp. 1157–1174.
- [38] R. LISKA AND B. WENDROFF, *Comparison of several difference schemes on 1D and 2D test problems for the Euler equations*, SIAM J. Sci. Comput., 25 (2003), pp. 995–1017.
- [39] H. LIU, *A numerical study of the performance of alternative weighted ENO methods based on various numerical fluxes for conservation law*, Appl. Math. Comput., 296 (2017), pp. 182–197.
- [40] R. LÖHNER, *An adaptive finite element scheme for transient problems in CFD*, Comput. Methods Appl. Mech. Eng., 61 (1987), pp. 323–338.
- [41] R. M. PIDATELLA, G. PUPPO, G. RUSSO, AND P. SANTAGATI, *Semi-conservative finite volume schemes for conservation laws*, SIAM J. Sci. Comput., 41 (2019), pp. B576–B600.

- [42] G. PUPPO AND M. SEMPLICE, *Numerical entropy and adaptivity for finite volume schemes*, Commun. Comput. Phys., 10 (2011), pp. 1132–1160.
- [43] J. QIU AND C.-W. SHU, *A comparison of troubled-cell indicators for Runge-Kutta discontinuous Galerkin methods using weighted essentially nonoscillatory limiters*, SIAM J. Sci. Comput., 27 (2005), pp. 995–1013.
- [44] C.-W. SHU, *High order weighted essentially nonoscillatory schemes for convection dominated problems*, SIAM Rev., 51 (2009), pp. 82–126.
- [45] ——, *Essentially non-oscillatory and weighted essentially non-oscillatory schemes*, Acta Numer., 29 (2020), pp. 701–762.
- [46] C.-W. SHU AND S. OSHER, *Efficient implementation of essentially non-oscillatory shock-capturing schemes*, J. Comput. Phys., 77 (1988), pp. 439–471.
- [47] V. A. TITAREV AND E. F. TORO, *Finite-volume WENO schemes for three-dimensional conservation laws*, J. Comput. Phys., 201 (2004), pp. 238–260.
- [48] E. F. TORO, *Riemann solvers and numerical methods for fluid dynamics*, Springer-Verlag, Berlin, third ed., 2009. A practical introduction.
- [49] B.-S. WANG AND W. S. DON, *Affine-invariant WENO weights and operator*, Appl. Numer. Math., 181 (2022), pp. 630–646.
- [50] B. S. WANG, W. S. DON, Z. GAO, Y. H. WANG, AND X. WEN, *Hybrid compact-WENO finite difference scheme with radial basis function based shock detection method for hyperbolic conservation laws*, SIAM J. Sci. Comput., 40 (2018), pp. A3699–A3714.
- [51] B.-S. WANG, W. S. DON, N. K. GARG, AND A. KURGANOV, *Fifth-order A-WENO finite-difference schemes based on a new adaptive diffusion central numerical flux*, SIAM J. Sci. Comput., 42 (2020), pp. A3932–A3956.
- [52] W. WANG, C.-W. SHU, H. C. YEE, D. V. KOTOV, AND B. SJÖGREEN, *High order finite difference methods with subcell resolution for stiff multispecies discontinuity capturing*, Commun. Comput. Phys., 17 (2015), pp. 317–336.
- [53] X. WEN, W. S. DON, Z. GAO, AND J. S. HESTHAVEN, *An edge detector based on artificial neural network with application to hybrid compact-WENO finite difference scheme*, J. Sci. Comput., 83 (2020). Paper No. 49.
- [54] P. WOODWARD AND P. COLELLA, *The numerical simulation of two-dimensional fluid flow with strong shocks*, J. Comput. Phys., 54 (1984), pp. 115–173.
- [55] Y. YANG, W. S. DON, Z. GAO, AND B.-S. WANG, *Hybrid compact-WENO scheme with RBF-FD based discontinuity detection method for hyperbolic conservation laws*, J. Numer. Methods Comput. Appl., 41 (2020), pp. 232–245.